Secondary Ice Production in Simulated Deep Convective Clouds: A Sensitivity Study

Cunbo Han,[a,b] Corinna Hoose,[a] and Viktoria Dürlich[a]

[a] *Institute of Meteorology and Climate Research, Karlsruhe Institute of Technology, Karlsruhe, Germany*
[b] *State Key Laboratory of Tibetan Plateau Earth System, Environment and Resources, Institute of Tibetan Plateau Research, Chinese Academy of Sciences, Beijing, China*

(Manuscript received 14 September 2023, in final form 19 January 2024, accepted 8 March 2024)

ABSTRACT: Multiple mechanisms have been proposed to explain secondary ice production (SIP), and SIP has been recognized to play a vital role in forming cloud ice crystals. However, most weather and climate models do not consider SIP in their cloud microphysical schemes. In this study, in addition to the default rime splintering (RS) process, two SIP processes, namely, shattering/fragmentation during freezing of supercooled rain/drizzle drops (DS) and breakup upon ice–ice collisions (BR), were implemented into a two-moment cloud microphysics scheme. Besides, two different parameterization schemes for BR were introduced. A series of sensitivity experiments were performed to investigate how SIP impacts cloud microphysics and cloud phase distributions in warm-based deep convective clouds developed in the central part of Europe. Simulation results revealed that cloud microphysical properties were significantly influenced by the SIP processes. Ice crystal number concentrations (ICNCs) increased up to more than 20 times and surface precipitation was reduced by up to 20% with the consideration of SIP processes. Interestingly, BR was found to dominate SIP, and the BR process rate was larger than the RS and DS process rates by four and three orders of magnitude, respectively. Liquid pixel number fractions inside clouds and at the cloud top decreased when implementing all three SIP processes, but the decrease depended on the BR scheme. Peak values of ice enhancement factors (IEFs) in the simulated deep convective clouds were 10^2–10^4 and located at −24°C with the consideration of all three SIP processes, while the temperature dependency of IEF was sensitive to the BR scheme. However, if only RS or RS and DS processes were included, the IEFs were comparable, with peak values of about 6, located at −7°C. Moreover, switching off the cascade effect led to a remarkable reduction in ICNCs and ice crystal mass mixing ratios.

SIGNIFICANCE STATEMENT: The cloud phase is found to have a significant impact on cloud evolution, radiative properties, and precipitation formation. However, the simulation of the cloud phase is a big challenge for cloud research because multiple processes are not well described or missing in numerical models. In this study, we implemented two secondary ice production (SIP) processes, namely, shattering/fragmentation during the freezing of supercooled rain/drizzle drops and breakup upon ice–ice collisions, which are missing in most numerical models. Sensitivity experiments were conducted to investigate how SIP impacts cloud microphysics and cloud phase in deep convective clouds. We found that SIP significantly impacts in-cloud and cloud-top phase distribution. We also identified that the collisional breakup of ice particles is the dominant SIP process in the simulated deep convective clouds.

KEYWORDS: Cloud microphysics; Secondary ice production; Cloud water/phase; Ice crystals; Deep convection

1. Introduction

Many clouds (so-called mixed-phase clouds) contain both liquid water droplets and ice crystals. Deep convective clouds are one of many types of mixed-phase clouds. As the cloud phase plays a critical role in cloud evolution, precipitation formation, and radiative properties on both regional and global scales (Korolev et al. 2017), it is of great importance to understand cloud microphysical processes, especially the ice formation processes in mixed-phase clouds. Supercooled cloud droplets freeze homogeneously when the temperature is below −38°C, while they nucleate heterogeneously with the help of aerosols serving as ice nucleating particles (INPs) in the temperature range between 0° and −38°C. In situ observations of mixed-phase clouds reveal that ice crystal number concentrations (ICNCs) are frequently larger than INP concentrations by orders of magnitude (Field et al. 2017; Lauber et al. 2021; Luke et al. 2021; Georgakaki et al. 2022). The ICNC–INP discrepancy has been attributed to unknown INP sources and secondary ice production (SIP) processes. However, SIP processes are still missing in most numerical weather and climate models. Therefore, introducing parameterizations of SIP processes in numerical models is critical for simulating cloud microphysics.

Multiple mechanisms have been proposed to account for SIP based on laboratory studies (Korolev and Leisner 2020), which are rime splintering (RS) or Hallett–Mossop process (Hallett and Mossop 1974), shattering/fragmentation during rain/drizzle drop freezing (DS) (Latham and Mason 1961; Dye and Hobbs 1968; Takahashi and Yamashita 1970; Lauber et al. 2018; Keinert et al. 2020), collisions between raindrops with more massive ice particles (Dye and Hobbs 1968; Phillips et al. 2017a, 2018; James et al. 2021), collisional breakup due to ice–ice collisions (BR) (Vardiman 1978; Takahashi et al. 1995), ice particle fragmentation

---

Denotes content that is immediately available upon publication as open access.

Corresponding authors: Cunbo Han, cunbo.han@itpcas.ac.cn; Corinna Hoose, corinna.hoose@kit.edu

DOI: 10.1175/JAS-D-23-0156.1

due to thermal shock (Gold 1963; Koenig 1963; Dye and Hobbs 1968), and fragmentation during sublimation (Oraltay and Hallett 1989). More and more simulation works have included the proposed SIP mechanisms (Sullivan et al. 2018a; Sotiropoulou et al. 2020; Zhao et al. 2021; Georgakaki et al. 2022; Huang et al. 2022; Waman et al. 2022). Recently, some studies treated many of the SIP processes, including RS, DS, BR, collision between raindrops with more massive ice particles, and fragmentation during sublimation (Patade et al. 2022; Waman et al. 2022; Gupta et al. 2023; Waman et al. 2023). Field et al. (2017) summarized the current states of SIP studies, including in situ observations, remote sensing, laboratory investigations, and modeling works. More recently, Korolev and Leisner (2020) reviewed the laboratory studies on SIP. Both reviews concluded that despite great efforts, the physical basis of the SIP mechanisms is still poorly understood, hindering the development of accurate parameterization of any of the proposed SIP processes (Field et al. 2017; Korolev and Leisner 2020).

Parameterization schemes for SIP are all developed based on laboratory observations. The rime splintering process is when supercooled liquid droplets rime onto ice particles and generate small ice splinters. Hallett and Mossop (1974) observed that ice splinters were generated in a temperature range from −8° to −3°C, and the maximum generation rate of ice splinters was at about −5°C. Many studies observed an enhanced ice particle number concentration in this temperature range (Harris-Hobbs and Cooper 1987; Bower et al. 1996; Taylor et al. 2016). Most of the parameterization schemes for the rime splintering process in numerical models are based on Hallett and Mossop's (1974) observations (Sullivan et al. 2018a; Sotiropoulou et al. 2021b). The rain/drizzle drop shattering/fragmentation process describes small ice fragments generated during the freezing of supercooled drops. Laboratory experiments have revealed that rain/drizzle drop shattering/fragmentation is active in a much broader temperature range, roughly below −10°C, and might be most efficient between −10° and −15°C (Field et al. 2017; Lauber et al. 2018; Korolev and Leisner 2020). The fragment generation rate is found to be related to temperature and droplet diameter. However, there are still no conclusions on the number of new splinters per fragmenting droplet (Keinert et al. 2020; Korolev and Leisner 2020), leading to difficulties in parameterizations of the rain/drizzle drop shattering/fragmentation process. Ice fragments are also produced due to a mechanical collision between two ice crystals, that is, the collisional breakup process. Vardiman (1978) and Takahashi et al. (1995) are the two first laboratory studies that investigated the collisional breakup process. A parameterization scheme developed by Fridlind et al. (2007) is based on Vardiman's (1978) observations, where the number of new fragments per collision is estimated as a function of momentum change ice particles. By fitting to Takahashi et al.'s (1995) experimental results, Sullivan et al. (2018a) developed a parameterization scheme for the number of new fragments, which depends only on temperature. Also, based on Takahashi et al.'s (1995) experiments, Phillips et al. (2017a) proposed a more comprehensive scheme for the mechanical breakup of ice–ice collisions based on the energy conservation principle. It was the first scheme to resolve all types of fragmentation observed individually by Vardiman (1978) and Takahashi et al. (1995), including collisions of either snow or crystals (dendritic and spatial planar) with any ice particles, collisions among graupel with other graupel/hail, and collisions among only hails. The scheme depends on collision kinetic energy, rimed fraction, temperature, and diameters of colliding particles.

The role of SIP in mixed-phase clouds has been extensively investigated using numerical simulations in recent years (Phillips et al. 2017b; Sullivan et al. 2017; Hoarau et al. 2018; Phillips et al. 2018; Sullivan et al. 2018a,b; Miltenberger et al. 2020; Sotiropoulou et al. 2020, 2021a,b; Zhao and Liu 2021; Zhao et al. 2021; Atlas et al. 2022; Georgakaki et al. 2022; Huang et al. 2022). Sullivan et al. (2017) performed idealized simulations using a six-hydrometeor-class parcel model and found that ICNC is enhanced by SIP by a factor of up to 10^4, and the most significant enhancement occurs for moderate updraft and cloud condensation nuclei (CCN) activation and ice nucleation rates. Including only the collisional breakup process, Phillips et al. (2017b) simulated a cold-based deep convective case observed over the U.S. High Plains using a hybrid bin-two-moment bulk microphysics scheme in 3D. Results indicated that ICNC increased by about one to two orders of magnitude, and it was also found that most of the breakup is due to collisions between snow and graupel/hail. Using a parcel model and six hydrometeor classes, Sullivan et al. (2018b) investigated the initiation of SIP. They concluded that the existence of a threshold concentration of primarily nucleated ice crystals is only necessary for the collisional breakup process, while cloud-base temperature and intensity of updraft are more critical for the initiation of rime splintering and rain/drizzle drop shattering/fragmentation processes. Sullivan et al. (2018a) found that ICNCs produced by SIP processes are as large as those from primary nucleation, and SIP processes intensify precipitation near convective regions of a rainband. Using a Lagrangian parcel model and a large-eddy simulation model, Sotiropoulou et al. (2020) showed that only the combination of rime splintering and collisional breakup processes could match the observed ICNCs for Arctic stratocumulus clouds. Later on, convection-resolving simulations with the Weather Research and Forecasting (WRF) Model by Sotiropoulou et al. (2021b) indicated that the collisional breakup process could explain the observed ICNCs in mixed-phase summer clouds over the Antarctic coast. Moreover, Georgakaki et al. (2022) argued that the collisional breakup process is relatively active in the simulation of orographic mixed-phase clouds in the Swiss Alps with the WRF Model, enhancing ICNCs by up to three orders of magnitude. However, Zhao et al. (2021) found that ice enhancement due to the fragmentation of freezing raindrops is the most significant at temperatures from −4° to −20°C in the simulated Arctic mixed-phase clouds. Huang et al. (2022) reported that the DS dominates ice production during the early stage of simulated tropical convective clouds. Waman et al. (2022) simulated a convective storm over the southern Great Plains and found that the BR process dominates ice production at long time scales and drives the ICNC toward a maximum. In summary, SIP processes have been verified to be of great importance in shaping different types of mixed-phase clouds. However, there are still debates on which SIP process dominates, and the importance of SIP processes is not well understood in different types of mixed-phase clouds.

For example, very few simulation studies focus on SIP impacts on deep convective clouds.

Cloud phase distribution of mixed-phase clouds impacts cloud radiative properties, cloud dynamics, and cloud lifetime. A lot of works have focused on the partitioning between ice and liquid and the phase transition from liquid to ice in mixed-phase clouds using numerical simulations and remote sensing retrievals (McCoy et al. 2016; Hoose et al. 2018; Coopman et al. 2020; Bruno et al. 2021; Coopman et al. 2021). Observations and simulations reveal that cloud phase distributions depend on not only temperature but also cloud type and SIP processes (Rosenfeld et al. 2011; Hoose et al. 2018). Unfortunately, physical processes that modulate cloud phase distribution in mixed-phase clouds are still poorly understood. Impacts of SIP on mixed-phase clouds in the polar regions have been extensively investigated by simulations and observations (Fu et al. 2019; Sotiropoulou et al. 2020; Luke et al. 2021; Sotiropoulou et al. 2021a; Pasquier et al. 2022). However, few works focus specifically on the phase distribution of mixed-phase deep convective clouds. Therefore, in this study, SIP processes (rime splintering, rain/drizzle drop shattering/fragmentation, and collisional breakup processes) are introduced into the Icosahedral Nonhydrostatic (ICON) model (Zängl et al. 2015). Sensitivity experiments are performed to investigate how and to what extent SIP processes impact cloud microphysics in deep convective clouds. In particular, we investigate how and to what extent SIP processes impact in-cloud and cloud-top phase distributions.

The paper is organized as follows: In section 2, we introduce the model setup and parameterization schemes for SIP; section 3 presents results and discussion; in section 4, we summarize this study and conclude.

2. Methodology

a. Model description

The ICON model (Zängl et al. 2015) is developed jointly by the German Weather Service (Deutscher Wetterdienst) (DWD), Max Planck Institute for Meteorology, German Climate Computing Center (Deutsches Klimarechenzentrum) (DKRZ), and Karlsruhe Institute of Technology (KIT). The ICON model is a unified model with three physics packages designed for numerical weather prediction (NWP), climate simulation, and large-eddy simulation (LES). ICON is a fully compressible model and solves prognostic variables on an unstructured triangular grid and with C-type staggering based on successive refinement of a spherical icosahedron (Gassmann and Herzog 2008; Wan et al. 2013). In this way, the singularity issues of the poles are solved, and the model performance is maximized as well. In the LES physics package of the ICON model (Dipankar et al. 2015), a three-dimensional subgrid-scale turbulence parameterization scheme based on the diagnostic Smagorinsky scheme is implemented. This scheme adapts Lilly's (1962) modifications for thermal stratification. In addition to the default diagnostic cloud fraction scheme, a simple all-or-nothing cloud scheme assuming the cloud fraction within a grid cell is either 1 or 0 is implemented for the LES package.

An updated version of the two-moment cloud microphysics scheme based on Seifert and Beheng (2006) is implemented in the ICON model, which predicts the number and mass mixing ratios of six hydrometeor types, including cloud droplets, rain droplets, cloud ice, snow, graupel, and hail. Hande et al.'s (2016) parameterization scheme for CCN activation is used to describe liquid droplet formation. Freezing of liquid water droplets and liquid aerosols via homogeneous freezing in ICON's two-moment microphysics scheme is parameterized by Kärcher et al.'s (2006) algorithm. Hande et al.'s (2015) parameterization scheme for heterogeneous ice nucleation is used, which includes immersion and deposition modes, and is formulated as a function of a temperature- and ice-supersaturation-dependent INP concentration. ICON's two-moment microphysics scheme allows for variable treatment of the ice habit for the cloud ice category. The generalized gamma distribution function was used to describe size distributions of hydrometeors. The diameter–mass [$D(x) \cong ax^b$] and fall-velocity–mass [$v(x) \cong \alpha x^{\beta}(\rho_0/\rho)^{\lambda}$] are parameterized by power laws, and the corresponding characteristic parameters are shown in Table 1.

b. Implementation of secondary ice production parameterizations

1) RIME SPLINTERING PARAMETERIZATION

A rime splintering parameterization is available by default in ICON's two-moment cloud microphysical scheme (Seifert and Beheng 2006). Note that small ice splinters break away during riming only for supercooled cloud droplets $> 24\ \mu$m. The tendency of ICNCs generated due to the rime splintering process is parameterized as a product of a leading coefficient, a temperature-dependent weighting function, and a rimed-ice mixing ratio:

$$\left.\frac{\partial N_{\text{ice}}}{\partial t}\right|_{\text{RS}} = \aleph_{\text{RS}} \times w_{\text{RS}}(T) \times q_{\text{rime}}, \tag{1}$$

where N_{ice} is the ICNC, q_{rime} is the rimed ice mixing ratio, $\aleph_{\text{RS}}$ is a constant and is set to 3.5×10^8 fragments per kilogram of rimed ice based on Hallett and Mossop's (1974) experiment, and $w_{\text{RS}}(T)$ is a temperature-dependent weighting for rime splintering and is triangular between 256 and 270 K, which is described as

$$w_{\text{RS}}(T) = \begin{cases} 0, & T < 256\ \text{K} \\ \dfrac{T - 256\ \text{K}}{3\ \text{K}}\dfrac{T - 270\ \text{K}}{-2\ \text{K}}, & 256\ \text{K} < T < 270\ \text{K}. \\ 0, & T > 270\ \text{K} \end{cases} \tag{2}$$

TABLE 1. Characteristic parameters for the ice particle maximum diameter $D(x)$ and the terminal fall velocity $v(x)$ of ice particles with mass x.

Ice type	a (m kg$^{-\beta}$)	b	α (m s^{-1} kg$^{-\beta}$)	β	λ
Cloud ice	0.835	0.39	27.7	0.216	0.5
Snow	5.130	0.5	8.294	0.125	0.5
Graupel	0.142	0.314	86.894	0.268	0.5
Hail	0.137	0.333	39.3	0.167	0.5

2) RAIN/DRIZZLE DROP FREEZING FRAGMENTATION PARAMETERIZATION

The rain/drizzle drop freezing shattering/fragmentation process is parameterized following Sullivan et al. (2018a) with the product of the freezing rate of the liquid droplet, a shattering/fragmentation probability P_{DS} that depends on temperature, and a constant fragment number $\aleph_{\mathrm{DS}}$:

$$\left.\frac{\partial N_{\mathrm{ice}}}{\partial t}\right|_{\mathrm{DS}} = (1 + p_{\mathrm{DS}}\aleph_{\mathrm{DS}})\frac{\partial N_{\mathrm{freeze}}}{\partial t}. \tag{3}$$

The shattering/fragmentation probability is given by a normal distribution in temperature, centered at a temperature T_μ and with a standard deviation σ:

$$p_{\mathrm{DS}} = \frac{p_{\max}}{\max[\mathcal{N}(T_\mu, \sigma)]}\mathcal{N}(T_\mu, \sigma), \tag{4}$$

$$\mathcal{N}(T_\mu, \sigma) = \frac{1}{\sqrt{2\pi}\sigma}\exp\left[\frac{-(T - T_\mu)^2}{2\sigma^2}\right], \tag{5}$$

where $p_{\max}$ is the maximum probability and has a value of 20%, temperature T_μ is 258 K, the standard deviation σ is 3 K, and the constant fragment number equals 10. The values are suggested by Sullivan et al. (2018b) in a simulation work performed with a parcel model.

3) COLLISIONAL BREAKUP PARAMETERIZATION

The collisional breakup process is parameterized as a product of fragment number ($\aleph_{\mathrm{BR}}$) and hydrometeor collision rate:

$$\left.\frac{\partial N_{\mathrm{ice}}}{\partial t}\right|_{\mathrm{BR},jk} = -\aleph_{\mathrm{BR}}\left.\frac{\partial N_j}{\partial t}\right|_{\mathrm{coll},jk}. \tag{6}$$

Two parameterization schemes for collisional breakup have been introduced: one was developed by Takahashi et al. (1995, hereafter TA95) and the other was developed by Phillips et al. (2017a, hereafter PH17). The fragment number in the TA95 scheme only depends on temperature:

$$\aleph_{\mathrm{BR}} = F_{\mathrm{BR}}(T - T_{\min})^{1.2}\exp[-(T - T_{\min})/\gamma_{\mathrm{BR}}], \tag{7}$$

where F_{BR} is a scaling factor with a value of 50, $T_{\min}$ is the lower temperature limit where no apparent fragmentation occurs, and γ_{BR} is the decay rate of fragmentation at warmer temperatures (Sullivan et al. 2018a). Note that TA95 used two ice spheres to conduct their experiments, and each ice sphere has a diameter of 18 mm. Thus, we introduced ice particle diameter information into the TA95 scheme:

$$\aleph_{\mathrm{BR}} = F_{\mathrm{BR}}(T - T_{\min})^{1.2}\exp[-(T - T_{\min})/\gamma_{\mathrm{BR}}] \times \frac{D_1 D_2}{D_0^2}, \tag{8}$$

where D_1 and D_2 are the mean diameters of two colliding ice particles and $D_0 = 18$ mm is the diameter of the ice balls used in TA95's experiments. A gamma distribution for ice hydrometeor types is used in ICON's two-moment microphysics scheme and the diameter for nonspherical ice particles is defined as the maximum diameter based on Locatelli and Hobbs (1974) and Heymsfield and Kajikawa's (1987) measurements. Sotiropoulou et al. (2021b) also included the influence of ice particle size in the TA95 scheme, but they assumed a linear dependency of the fragment number on ice particle diameter.

The PH17 scheme is based on the collision kinetic energy of two colliding particles and varies with ice particle type and habit, which is more physical:

$$\aleph_{\mathrm{BR}} = \alpha A\left\{1 - \exp\left[-\left(\frac{CK_0}{\alpha A}\right)^\gamma\right]\right\}, \tag{9}$$

where α is the equivalent spherical surface area of the smaller particle, A is the density of breakable branches at the surface, C is the asperity fragility coefficient, and γ is a shape parameter. Parameters A, C, and γ depend on collision types. The values of these parameters are different for different colliding particle pairs, and the details are found in appendix and Table 1 in PH17. The term K_0 is the collision kinetic energy and is a function of mass and terminal velocities of colliding particles:

$$K_0 = \frac{1}{2}\frac{m_j m_k}{m_j + m_k}(v_j - v_k)^2, \tag{10}$$

and more details are found in PH17. To avoid vanishing relative differences by using the mean values of particle size distribution in ICON's two-moment bulk microphysics, the following equation is used to calculate the characteristic collision velocity difference:

$$(v_j - v_k)^2 = \vartheta_j^0 v_j^0 - \vartheta_{jk}^1 v_j v_k + \vartheta_k^1 v_k^2 + \sigma_j^2 + \sigma_k^2, \tag{11}$$

where ϑ_j^m are dimensionless coefficients and σ_j and σ_k are the variances of the velocity distributions of the two colliding hydrometeor types (Seifert and Beheng 2006). The PH17 scheme is more suitable for implementing in spectral bin microphysics schemes, which predict hydrometeor concentrations in each size interval. Nevertheless, bin microphysics schemes are computationally expensive, and numerical weather and climate models typically employ bulk microphysics schemes. Fortunately, the PH17 scheme can also be applied in bulk microphysics schemes by adopting an emulated bin microphysics approach for the ice–ice collisions (PH17). In this study, temporary bins for each colliding ice particle were constructed to discretize the ice size distribution, which is assumed to follow a gamma distribution in the bulk microphysics. Subsequently, the BR process was applied to each permutation of bin sizes, and the resulting fragments were summed up over all bin pairs.

There are four ice hydrometeor classes: ice crystal, snow, graupel, and hail. SIP is allowed after collisions between ice and snow, ice and graupel, ice and hail, snow and snow, snow and graupel, snow and hail, graupel and graupel, and graupel and hail. Note that only the PH17 scheme actually resolves these permutations of collisions, since it treats colliding ice particle pairs differently and concentrations in each size bin are emulated. Particles having diameters 500 μm $< D <$ 5 mm are allowed for breakup upon collisions. Generated fragments are recognized as small ice crystals and are added to the cloud ice category. Mass and number concentrations are redistributed in the two colliding ice classes. In this study, only collision between cloud ice crystals is prohibited and permutations of collisions between other ice particles are all allowed. PH17 and Phillips et al. (2017b) also enabled all types of collisions between all ice particles. However, in Sotiropoulou et al.'s (2021a) study, collisions between ice particles and hail are missing due to no hail species in their cloud microphysical scheme.

4) QUANTIFICATION OF THE CASCADE EFFECT

Ice multiplication as a chain-reaction-type mechanism was proposed by Koenig (1963) to explain the rapid growth of ice particles in summer cumulus clouds. This chain-reaction-type mechanism is here called the cascade effect, which describes small ice crystals colliding or riming with other large liquid drops or ice particles which in turn produce more small ice crystals. While the cascade effect is active in nature and in modeling studies including SIP processes in cloud microphysics, only a few studies have explicitly investigated the cascade effect (Lawson et al. 2015; Sullivan et al. 2018a) due to the difficulty in observation and quantification. In this study, with the help of numerical simulations, the cascade process is switched on and off by either allowing the ICNC tendencies parameterized via Eqs. (1), (3), and (6) to feed back onto ICNC, or to use these equations purely diagnostically, and their effects on cloud microphysics are investigated.

c. *Model configuration and simulation experiments*

Two types of simulation experiments are conducted in this study, realistic NWP simulations, which use Reynolds-averaged Navier–Stokes for a case of deep convective clouds (DCC) over Europe, and idealized LES, which resolve large eddies explicitly, for a case from the Convectional Precipitation Experiment (COPE) campaign (Leon et al. 2016; Lasher-Trapp et al. 2018). The model setup of the NWP simulations for the DCC case is the same as Han et al. (2023). A two-layer nested domain is used with one-way nesting, and the domain covers a major part of central Europe (Fig. 1). The horizontal resolution for the nested domains is halved from 2400 to 1200 m in the innermost domain, and the time steps for the two domains are 12 and 6 s, respectively. One hundred fifty vertical levels, with a grid stretching toward the model top at 21 km, are used. The vertical resolution is the same for all horizontal resolutions, and the lowest 1000 m encompasses 20 layers. A 1D vertical turbulence diffusion and transfer scheme is used for the 2400- and 1200-m resolutions. Deep convection is explicitly resolved, and shallow convection is parameterized for both domains. The simulations are initialized at 0000 UTC from ICON model configured over Europe (ICON-EU) analyses and integrated for 24 h. At the lateral boundaries of the outer domain, the simulation of the model is updated with 3-hourly ICON-EU analyses. The nested domains are coupled online, and the outer domain provides lateral boundary conditions to the inner domain. The day 6 June 2016 was selected to simulate because summertime deep convective clouds developed in central Europe (Han et al. 2023). Spatial distributions of retrieved cloud-top temperature (CTT) and cloud phase (CPH) at 1300 UTC for the Cloud Property Dataset Using Spinning Enhanced Visible and Infrared Imager (SEVIRI), edition 2 (CLAAS-2), satellite observations and DCC_CTRL case are shown in Fig. 2. As illustrated in Fig. 2, multiple well-developed isolated deep convective clouds are scattered in the domain with a typical horizontal scale of more than 100 km. Although the horizontal extent and intensity of individual convective clouds are not well reproduced, the ICON simulation generally captures the location of cores of the deep convective clouds, CTT, and CPH. The maximum cloud-top height reached more than 12 km (AGL), accompanied by a CTT of lower than −60°C at 1300 UTC. The average cloud-base height is approximately 2.8 km (AGL), with a cloud-base temperature of 1.6°C from 0900 to 1900 UTC. Therefore, CTT spanned the entire range from above 0°C to below the homogeneous freezing temperature, allowing for the activation of all considered SIP mechanisms. As the cloud-base temperature is similar to that of the cold-based clouds studied by Gupta et al. (2023), for which a dominance of cold precipitation formation over warm-rain processes was found, we expect a similar behavior for our case.

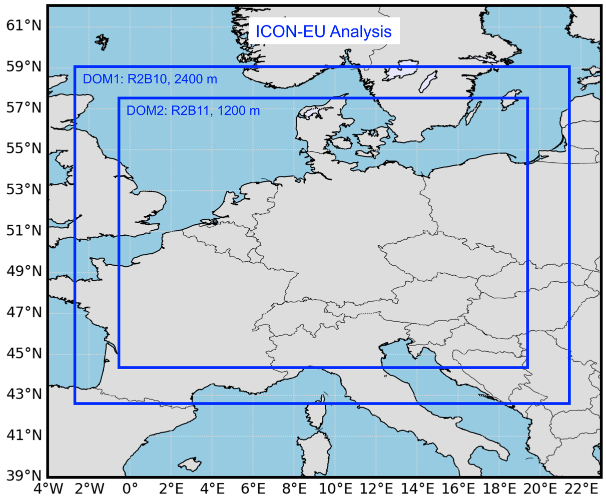

FIG. 1. The nested simulation domain for the NWP simulation of the DCC case.

The horizontal domain of idealized LES simulations extends 36 km in an east–west direction and 63 km in a south–north direction and has a horizontal grid spacing of 150 m. In the vertical direction, the first level is at 10-m altitude, whereas all other levels have 150-m thickness up to a model top of 10 km. A 1.0-s time step was used, and double periodic lateral boundary conditions were applied. The initial profiles of temperature, specific humidity, and horizontal wind were adapted from the radiosonde observations from the COPE campaign on 2 August 2013 in southwestern England (Leon et al. 2016; Lasher-Trapp et al. 2018) and are shown in Fig. 3a. Deep convective clouds were triggered by a series of warm bubbles imposed at $x = 9$ km and $y = 4$, 10, 16, and 22 km and initiated at $t = 100$, 200, 300, and 400 s from the simulation start. All warm bubbles have a horizontal radius of 2.5- and 1.2-km vertical depth. This configuration mimics the storm with a line of convective cells observed on 2 August 2013 during the COPE experiment. A depth of about 1.5-km damping layer was imposed below the domain top to reduce the reflection and buildup of gravity waves. Random perturbations into the initial potential temperature field were applied to trigger turbulence. This model configuration and the initial profiles were suggested for the COPE deep Cu case

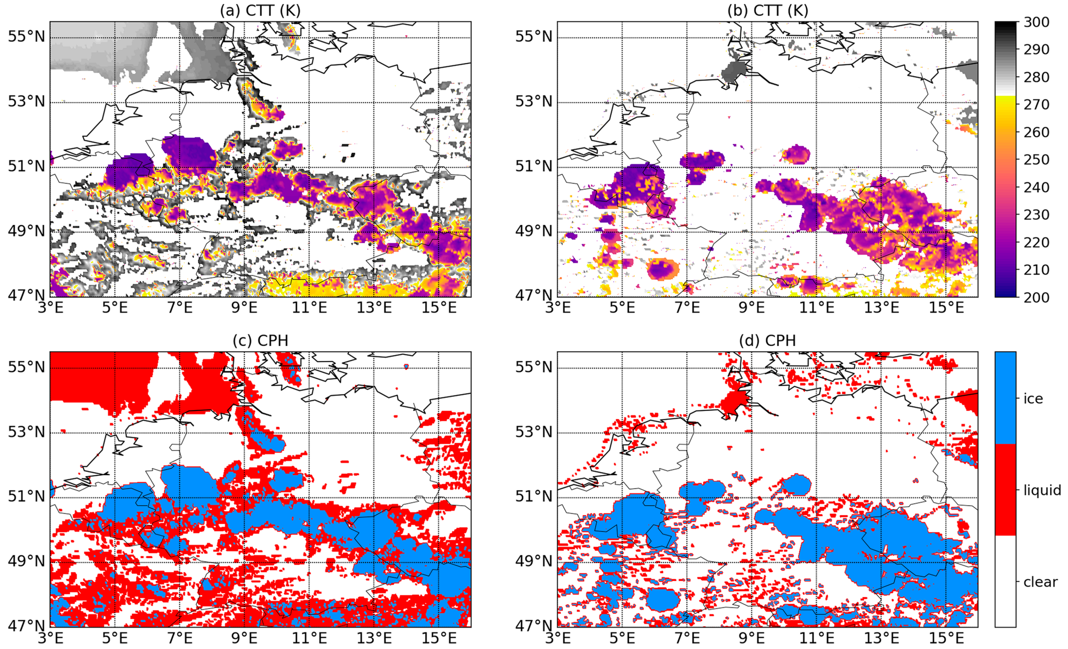

FIG. 2. Spatial distributions of the retrieved CTT and CPH at 1300 UTC for the NWP DCC case. (left) The CLAAS-2 product (Stengel et al. 2014; Benas et al. 2017) and (right) the NWP DCC_CTRL case.

of the 10th International Cloud Modeling Workshop (see details in https://iccp2020.tropmet.res.in/Cloud-Modeling-Workshop-2020).

This study conducts a series of sensitivity simulations that gradually introduce rime splintering, rain/drizzle drop shattering/fragmentation, and collisional breakup processes using NWP physics (Table 2). The DCC_CTRL experiment uses the default ICON 2-moment microphysics, in which only RS is considered for SIP. In the experiment DCC_SIP_NO, all SIP processes are switched off. DCC_RS+DS considers both RS and DS processes. DCC_BR_TA and DCC_BR_PH are two cases that only include the BR process for SIP, and TA95 [Eq. (7)] and PH17 parameterization schemes are used, respectively. DCC_SIP_TA, DCC_SIP_TA-D, and SIP_PH consider all three SIP processes, while using TA95 [Eq. (7)], diameter adjusted TA95 [Eq. (8)], and PH17 schemes for the BR mechanism, respectively. Moreover, the sensitivity of SIP to RS is investigated by scaling the RS intensity. The RS process rate is multiplied with a constant of 10, creating an additional case named DCC_RS10. One case using the same scheme for SIP processes as DCC_SIP_PH but with cascade effect switched off is performed, which is DCC_SIP_PH_NCS. Moreover, we simulate additional experiments with LES physics, a higher spatial resolution (150 m in horizontal directions), and lower cloud top (also lower vertical velocities) to check for the consistency of the results regarding the relative

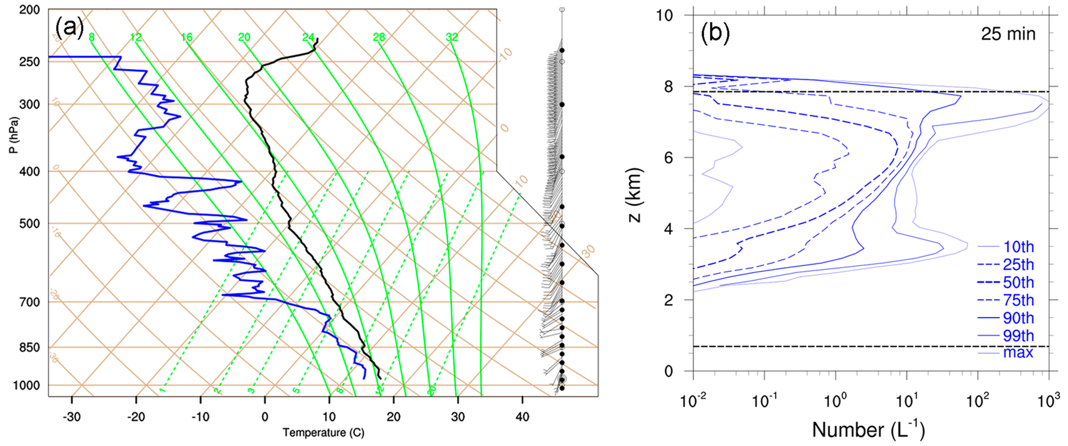

FIG. 3. (a) Radiosonde profiles from the COPE experiment on 2 Aug 2013 (Lasher-Trapp et al. 2018) and (b) the contoured-frequency-by-altitude diagrams of total ice number concentration for the COPE_CTRL case at 25 min. The horizontal black dashed lines in (b) indicate the cloud-top and cloud-base heights.

TABLE 2. List of experiments conducted in this study.

Physics	No.	Experiment	SIP
NWP	1	DCC_CTRL	RS
	2	DCC_SIP_NO	No SIP
	3	DCC_RS+DS	RS, DS
	4	DCC_BR_TA	BR, TA95's BR scheme [Eq. (7)]
	5	DCC_BR_PH	BR, Phillips et al.'s (2017a) BR scheme [Eq. (9)]
	6	DCC_SIP_TA	RS, DS, BR, TA95's BR scheme [Eq. (7)]
	7	DCC_SIP_PH	RS, DS, BR, Phillips et al.'s (2017a) BR scheme [Eq. (9)]
	8	DCC_SIP_TA-D	RS, DS, BR, TA95's BR scheme with diameter adjustment [Eq. (8)]
	9	DCC_RS10	RS process is scaled by multiplying by 10
	10	DCC_SIP_PH_NCS	Same as SIP_PH but without cascade effect
LES	11	COPE_CTRL	RS
	12	COPE_SIP_TA	RS, DS, BR, TA95's BR scheme [Eq. (7)]
	13	COPE_SIP_PH	RS, DS, BR, Phillips et al.'s (2017a) BR scheme [Eq. (9)]
	14	COPE_SIP_TA-D	RS, DS, BR, TA95's BR scheme with diameter adjustment [Eq. (8)]

importance of the SIP processes. Three cases including all the three SIP processes are selected, which are the COPE_SIP_TA, COPE_SIP_TA-D, and COPE_SIP_PH.

A large amount of cloud physics and aerosol data were collected during the COPE using ground-based and airborne radar measurements (Leon et al. 2016). Despite the highly idealized setting in the simulations, the LES results from this study were compared to observations from COPE. The control run (COPE_CTRL) generally agreed with the observed features of clouds and precipitation. The clouds developed along the series of warm bubbles, matured, and dissipated during the 2-h simulations. The cloud started to precipitate 25 min after the start of the simulation and the cloud lifetime was approximately 1 h. The simulated cloud-base height is approximately 550 m and the maximum cloud-top height is about 7.8 km, which are consistent with the observations (Taylor et al. 2016; Jackson et al. 2018). The vertical profile of total ice cloud number concentration at 25 min for the control run is shown in Fig. 3b. During the development stage (15 min) of convections, ice particles were mainly generated through primary ice nucleation. Over time, ice particles gradually increased, particularly within the rime-splintering temperature range. The trend in ice crystal number concentration aligns with in situ observations (Taylor et al. 2016; Jackson et al. 2018) and is also consistent with simulations by Lasher-Trapp et al. (2018). In particular, the simulated ice crystal number concentration was as high as several hundred per liter, which is also consistent with in situ observations by Taylor et al. (2016) and Jackson et al. (2018). The convection simulations in this study reproduce some features in the observations, regarding convection development, cloud-base/top heights, and ice crystal number concentration. However, the idealized nature of the simulations makes direct and detailed comparison with in situ measurements remain problematic.

3. Results and discussion

a. SIP importance for cloud microphysical properties

The importance of SIP for cloud microphysical properties is revealed by comparing results from the series of sensitivity experiments. Significant differences are found in the spatial and time-averaged profiles of the number concentrations and mass mixing ratios of cloud hydrometeors, as shown in Fig. 4. The profiles discussed here are averaged over cloudy pixels and from 0900 to 1900 UTC when the deep convective clouds are well developed. Only pixels with a total condensate mass greater than a threshold of 1.0×10^{-5} kg kg^{-1} are recognized as cloudy pixels. Note that the features of simulated convective clouds are comparable to the satellite observations shown in Fig. 2, and the convective updrafts are relatively strong, with the maximum vertical velocity of updrafts exceeding 25 m s^{-1} in the mature stage. Compared to DCC_SIP_NO, introducing the RS process (case DCC_CTRL) or RS and DS processes (case RS+DS) does not significantly impact the total ICNCs (Fig. 4a). The ICNC increases strongly after introducing the BR process by a factor of 4 in DCC_BR_PH, DCC_SIP_PH, and DCC_SIP_TA-D and by a factor of more than 20 in DCC_BR_TA and DCC_SIP_TA compared to the reference run (case DCC_CTRL). The mass mixing ratio of total ice decreases slightly after including RS and DS processes (case DCC_RS+DS) compared to DCC_SIP_NO and DCC_CTRL (Fig. 4d). Moreover, the peak of spatial and time-averaged cloud ice mass mixing ratio profile increases from 0.11 g kg^{-1} in SIP_NO to 0.19 g kg^{-1} in DCC_SIP_TA by more than 70%. This suggests that SIP by the BR process is more intensive than that by the RS and DS processes in our simulated deep convective clouds. The number concentrations and mass mixing ratios of cloud and rainwater are also greatly influenced by introducing SIP processes. Cloud water number concentrations and mass mixing ratios decrease in the upper part of clouds after including the SIP processes (Figs. 4b,e). The surface rainwater decreases significantly after introducing the SIP processes, especially in DCC_SIP_TA and DCC_BR_TA. It reduces from 0.018 g kg^{-1} in the reference run (case DCC_CTRL) to 0.014 g kg^{-1} in DCC_BR_TA by more than 20% (Fig. 4f).

To further identify the dominant one among the three SIP processes, we diagnosed the process rates (ice mass mixing ratio tendencies) for the three SIP processes. Figure 5a shows the spatial and time-averaged process rates of RS, DS, and BR over cloudy pixels from 0900 to 1900 UTC for cases DCC_SIP_TA, DCC_SIP_PH, and DCC_SIP_TA-D from

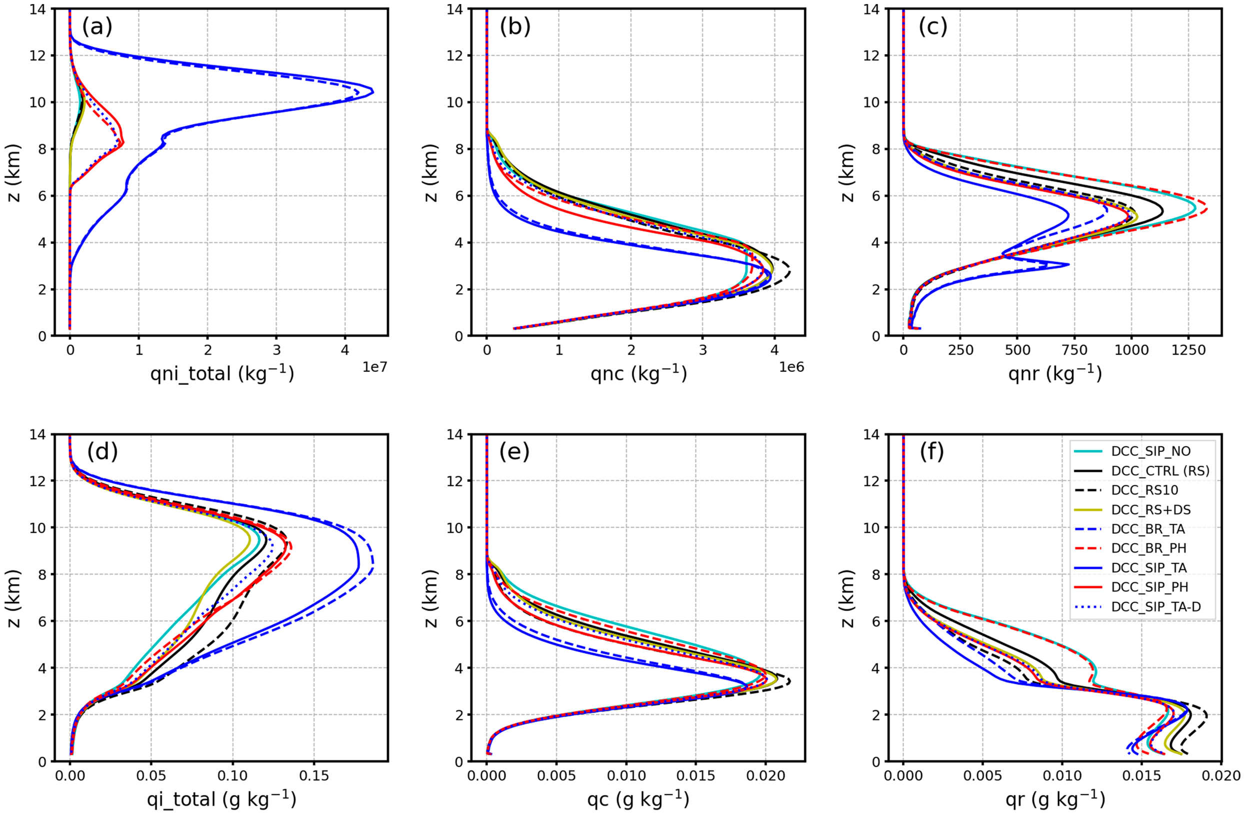

FIG. 4. Spatial and time-averaged (from 0900 to 1900 UTC) profiles over cloudy pixels of number concentration of (a) total cloud ice, (b) cloud liquid water and (c) rainwater, and profiles of mass mixing ratio of (d) total cloud ice, (e) cloud liquid water, and (f) rainwater for the NWP DCC cases.

the NWP simulations. In the DCC_SIP_TA case, the peak of the RS process rate profile is at about 4.2 km (corresponding to about −5°C), the peak of the DS process rate profile is higher at about 6.5 km, and the peak of the BR process rate profile is pretty broad, ranging from about 4 to 8 km. The peak value of the BR process rate is larger than that of the DS process rate by about three orders of magnitude and is larger than the peak value of the RS process rate by about

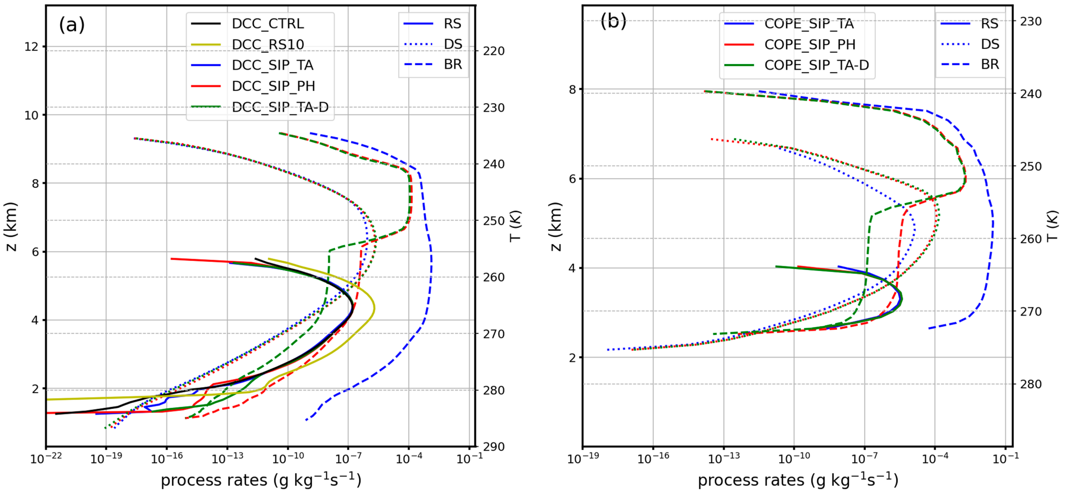

FIG. 5. Spatial and time-averaged profiles of process rates for cloudy pixels of RS, DS, and BR for (a) the NWP DCC simulations and (b) the idealized LES case (COPE).

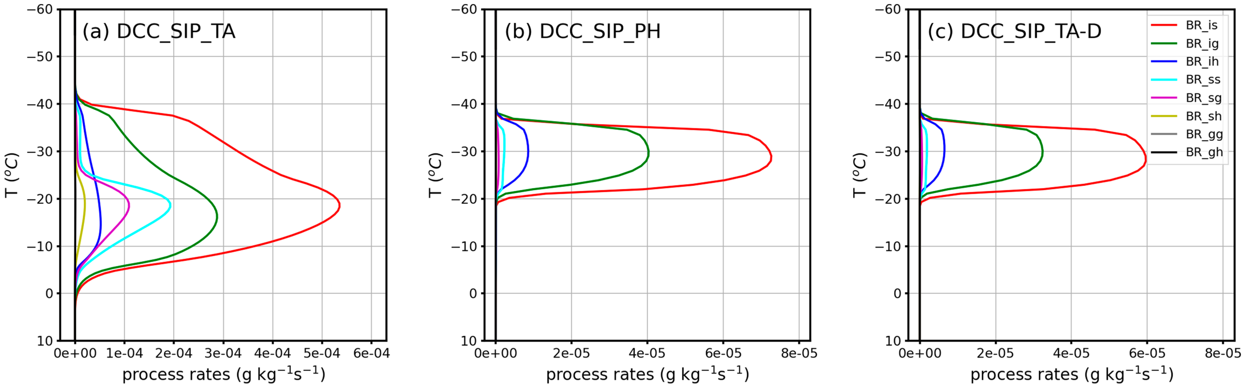

FIG. 6. Spatial and time-averaged profiles of process rates for cloudy pixels of the BR process between ice and snow (BR_is), ice and graupel (BR_ig), ice and hail (BR_ih), snow and snow (BR_ss), snow and graupel (BR_sg), snow and hail (BR_sh), graupel and graupel (BR_gg), and graupel and hail (BR_gh) for (a) DCC_SIP_TA, (b) DCC_SIP_PH, and (c) DCC_SIP_TA-D cases (NWP DCC simulations).

four orders of magnitude. A similar phenomenon happens in DCC_SIP_PH and DCC_SIP_TA-D. The BR process rate in the DCC_SIP_TA case differs significantly from that in DCC_SIP_PH and DCC_SIP_TA-D. The BR process rate in DCC_SIP_TA is larger than that in DCC_SIP_PH and DCC_SIP_TA-D by about 4.5 and 5.5 orders of magnitude below 6.5 km, respectively. However, the three BR process rates converge above 7 km. Note that the BR process rate in DCC_SIP_PH is larger than that in DCC_SIP_TA-D by about one order of magnitude below 6.0 km, while the two BR process rates are identical above 6.0 km.

Some studies argue that RS is a critical process responsible for the SIP and the RS process is the first SIP process that has been studied in laboratories and introduced into numerical models (Hallett and Mossop 1974; Koenig and Murray 1977; Lasher-Trapp et al. 2021; Luke et al. 2021). However, there are large uncertainties in numerical models regarding the parameterization of the RS process. To further identify the influence of the RS process, in this study, the RS intensity is scaled with a factor of 10 (case DCC_RS10), and its impacts on cloud microphysics are analyzed. The process rate of mass mixing ratio increases in DCC_RS10, as expected, by about one order of magnitude compared to CTRL (Fig. 5a). The peak value of the process rate is also located at about 4.2 km, corresponding to about −5°C. However, the spatial and time-averaged vertical profile for ICNC is almost identical in DCC_RS10 compared to DCC_CTRL (Fig. 4a). The ice crystal mass mixing ratio profile behaves differently from the ICNC profile, and ice mass mixing ratio increases from 3 to about 9 km in DCC_RS10 compared to DCC_CTRL. Interestingly, cloud liquid water mass and number concentration and surface precipitation increase slightly with increasing RS intensity. In general, increasing RS intensity, even with an extreme factor 10, has limited impacts on cloud microphysics, and the impacts are not as significant as the DS and BR processes.

As the sensitivity to the BR parameterization was found to be strong in the NWP simulations, three additional LES experiments were conducted to test whether a similar sensitivity exists also in this case, which are cases COPE_SIP_TA, COPE_SIP_PH, and COPE_SIP_TA-D. The process rates of SIP for the three LES cases are shown in Fig. 5b. The peak values of the BR process rate profile are larger than RS and DS by four and three orders of magnitude, respectively, which is consistent with the realistic simulations. Again, the peak value of the BR process rate from COPE_SIP_TA is in a wide temperature range, from about 2.5 to 7 km. The peak values of the BR process rates in COPE_SIP_PH and COPE_SIP_TA-D are higher and narrower from about 5.5 to 7 km. The vertical structures of RS, DS, and BR process rate profiles are quite similar between the realistic simulation of the NWP DCC case and the idealized simulation of the COPE case.

The BR process rates between different colliding particles for cases DCC_SIP_TA, DCC_SIP_PH, and DCC_SIP_TA-D are plotted in Fig. 6. BR processes are activated in a wide temperature range between 0° and −38°C in DCC_SIP_TA, with the peaks of BR process rates occurring approximately in between −15° and −20°C. The characteristics of the vertical profile and peak of BR process rates in DCC_SIP_TA case are mainly dominated by the temperature thresholds. Interestingly, in DCC_SIP_PH and DCC_SIP_TA-D, BR processes are activated in a narrower temperature range between −18° and −38°C, with the peaks located at approximately in between −25° and −30°C. The characteristics of the vertical profile of BR process rates are dominated not only by temperature but also by ice particle mass and diameter in DCC_SIP_PH and DCC_SIP_TA-D cases. The most significant BR process is the collision between ice and snow particles in all three cases, and the second most significant BR process is the collision between ice and graupel. Moreover, all the BR process rates in DCC_SIP_TA are larger than those in cases DCC_SIP_PH and DCC_SIP_TA-D by about one order of magnitude. Note that the BR process rates in DCC_SIP_PH and DCC_SIP_TA-D are highly consistent in terms of vertical structure, while the values of process rates are slightly different.

There is a long debate on which SIP process is dominant. Recently, multiple studies revealed that the BR process could explain the observation of enhanced ICNCs. Sotiropoulou et al. (2021b) found that the RS mechanism is relatively weak in the WRF Model while including the BR process could account for the observed ICNCs in the simulated Antarctic mixed-phase clouds. Georgakaki et al.'s (2022) simulation work reported that

BR is more active than DS in elevating the predicted ICNCs in orographic mixed-phase clouds in the Swiss Alps. Waman et al. (2022) suggested that the BR process dominates ice concentration above −15°C in a simulated continental convective storm and contributes about 70% to the ice concentration produced by SIP processes. Dedekind et al. (2021) also reported that the BR process is more significant than RS in increasing ICNCs in their simulation work of winter orographic mixed-phase clouds around Gotschnagrat in the Davos region in Switzerland. Our findings are consistent with these studies, although we simulate a different cloud type. Moreover, whether SIP processes stimulate or suppress surface precipitation is still undetermined. Georgakaki et al. (2022) found that surface precipitation was increased by as much as 30% after including SIP processes. However, Dedekind et al. (2021) reported that enhanced ICNCs reduced the regions of strong surface precipitation due to the BR process. We find the surface precipitation is reduced by as much as 20% when including the SIP processes, which is inconsistent with previous findings (Phillips et al. 2017b; Hoarau et al. 2018; Gupta et al. 2023), where deep convective clouds were also simulated. The relative importance of the three SIP processes and their influences on surface precipitation seem to depend on cloud types. In the future, more cloud types under different synoptic conditions need to be investigated to consolidate this conclusion.

b. *Sensitivity of cloud phase to SIP*

The ratio between the cloud droplet mixing ratio and the sum of the cloud droplet mixing ratio and ice crystal mixing ratio is defined as the cloud liquid mass fraction. Figures 7a–c show the scatterplots of in-cloud liquid mass fraction versus temperature sampled at a time interval of 15 min between 0900 and 1900 UTC of cloudy pixels for cases DCC_CTRL, DCC_SIP_TA, and DCC_SIP_PH. Figures 7d–f show the occurrence frequency of the points for the three cases. Generally, pure liquid and mixed-phase pixels are reduced significantly in DCC_SIP_TA and DCC_SIP_PH compared to the reference case DCC_CTRL, which includes only the RS process. In the meantime, the number of pure ice pixels increases greatly in DCC_SIP_TA and DCC_SIP_PH. These are caused by the SIP via DS and BR processes and are most likely reinforced by the Wegener–Bergeron–Findeisen (WBF) process and riming. As a consequence of the higher ICNCs produced in DCC_SIP_TA, the simulated cloud phase distributions between DCC_SIP_TA and DCC_SIP_PH are significantly different. In DCC_SIP_TA, there are already a large number of pixels with liquid fraction below 0.5 and even reaching 0.0 slightly below 0°C. Moreover, there are very few mixed-phase pixels ($0.0 <$ liquid fraction < 1.0) below −20°C in DCC_SIP_TA, which is quite different from DCC_SIP_PH.

Figure 8 shows the scatterplots of cloud-top liquid mass fraction against temperature and the occurrence frequency of the values. The cloud top is defined as the uppermost cloudy pixel (total condensate mass greater than 1.0×10^{-5} kg kg^{-1}) of one atmospheric column. Vertical velocity at the cloud top is smaller than within the cloud, and a large number of pixels have a negative vertical velocity (sinking motion). The number of pure liquid and mixed-phase pixels is reduced significantly, while the number of pure ice pixels increases in DCC_SIP_TA and DCC_SIP_PH due to the DS and BR processes. This is similar to inside the cloud. In DCC_SIP_TA, many pixels have a low liquid fraction, even reaching 0.0 already slightly below 0°C, and very few points have a liquid fraction between 0.5 and 1.0 below −10°C. This is significantly different from DCC_SIP_PH and DCC_CTRL.

A binary cloud phase assumption for cloudy pixels is derived following earlier studies (Hoose et al. 2018; Han et al. 2023) to mimic satellite products of the cloud-top phase. A cloudy pixel having a liquid mass fraction larger than 0.5 is recognized as a liquid pixel. Otherwise, it is counted as an ice pixel. The ratio of the number of liquid pixels to the total number of cloudy pixels is defined as the liquid cloud pixel number fraction. In-cloud and cloud-top liquid pixel number fractions against temperature for experiments are shown in Fig. 9. Only including RS and DS processes has a negligible influence on the liquid pixel number fraction (case DCC_RS+DS) (Fig. 9a). Switching off all the SIP processes leads to an increase in liquid pixel number fraction (case DCC_SIP_NO) compared to the reference DCC_CTRL case. However, the liquid pixel number fraction inside clouds drops significantly in the temperature range between −5° and −30°C after including the BR process (Fig. 9a). In line with Figs. 7 and 8, liquid pixel number fractions in DCC_SIP_TA and DCC_BR_TA start to decrease immediately below 0°C, while in other cases, liquid pixel number fractions begin to decrease at about −5°C. The in-cloud glaciation temperature, at which the liquid cloud pixel number fraction is equal to 0.5, shifts toward a warmer temperature by about 5°C in DCC_SIP_PH and by 13°C in DCC_SIP_TA and DCC_BR_TA cases compared to the DCC_CTRL case. At the cloud top, the liquid pixel number fractions in DCC_SIP_TA, DCC_BR_TA, and DCC_SIP_TA-D decrease in the temperature range between 0° and −20°C (Fig. 9b) and are more noisy compared to in-cloud due to a smaller number of pixels. The cloud-top glaciation temperature shifts toward a warmer temperature by about 10°C in DCC_SIP_TA and DCC_BR_TA and by about 3°C in DCC_SIP_TA-D. However, the liquid pixel number fraction differences between cases DCC_SIP_PH, DCC_BR_PH, and DCC_CTRL are not significant.

To summarize, we found that the in-cloud and cloud-top phase distribution is very sensitive to SIP processes in the mixed-phase temperature range. Liquid mass fraction and liquid pixel number fraction decrease significantly inside clouds and at the cloud top if all three SIP processes are introduced, especially the collisional breakup process. Phillips et al. (2017b) and Waman et al. (2022) also reported that ice number concentration is sensitive to the ice–ice collision process in the middle and upper half of the mixed-phase region. Moreover, large uncertainties exist in simulating the cloud phase with different parameterization schemes of SIP processes. The TA95 scheme produces ice particles more efficiently than PH17, leading to a lower liquid pixel number fraction inside clouds and at the cloud top as well as much higher glaciation temperatures. However, if TA95 is scaled by ice particle diameter, its simulation results are comparable to PH17. Cloud phase distributions are the observable properties of clouds, with constraints available both from in situ observations (Korolev et al. 2003) and from satellites (Bruno et al. 2021). Although there are no in situ observations

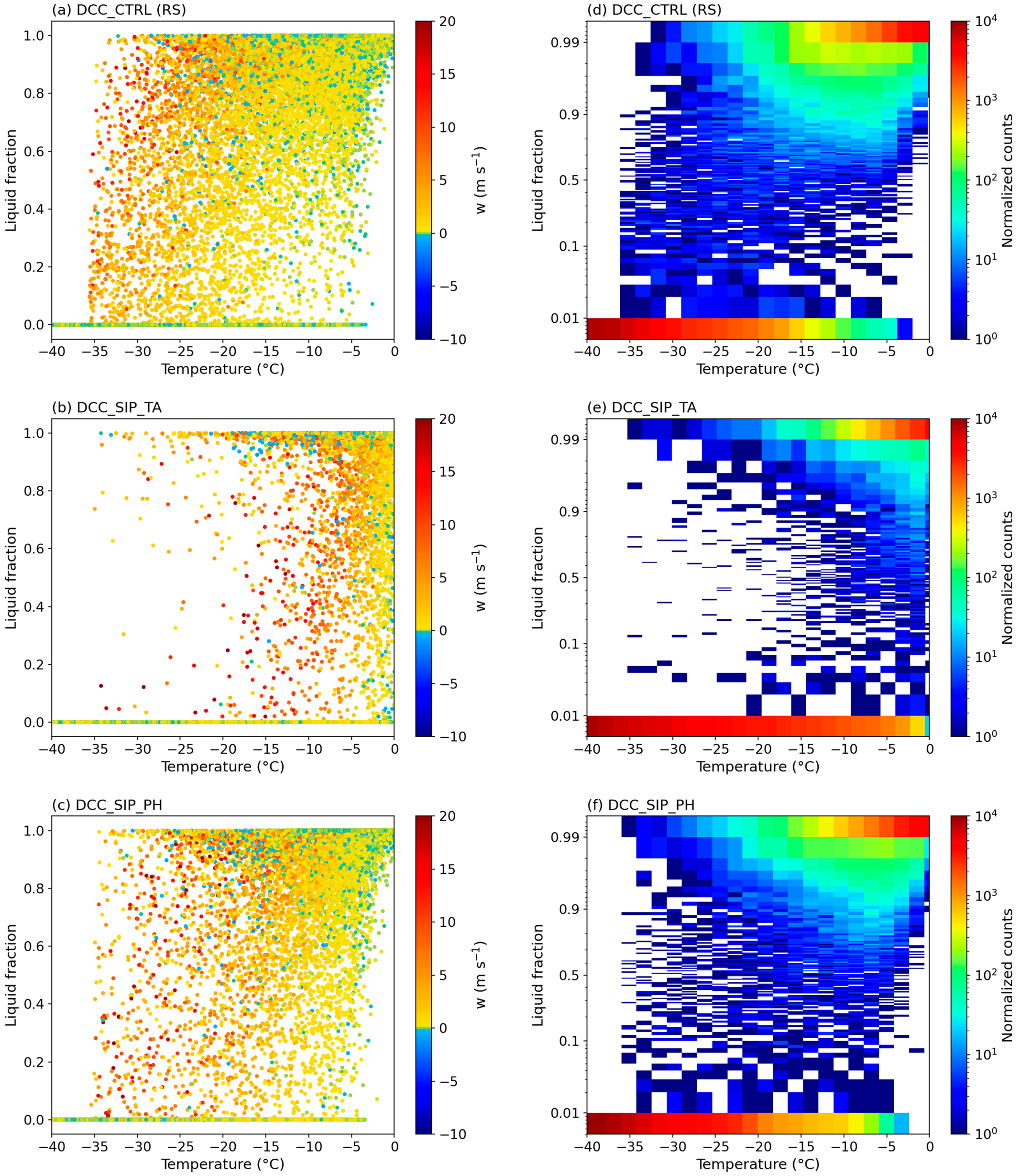

FIG. 7. In-cloud supercooled liquid water mass fraction distribution as a function of temperature between 0900 and 1900 UTC for cases (a) DCC_CTRL, (b) DCC_SIP_TA, and (c) DCC_SIP_PH. The color of points indicates vertical velocity (m s^{-1}), where warm colors represent ascending motion, and cool colors signify sinking motion. The 2D histogram of in-cloud liquid mass fraction vs temperature for cases (d) DCC_CTRL, (e) DCC_SIP_TA, and (f) DCC_SIP_PH. The temperature is binned by 1°C. The colors represent the normalized counts of data points (the number of data points is scaled to the $[10^0, 10^4]$ range).

available for the simulated cases, it can be stated that the results obtained with the TA95 scheme (without diameter scaling) are not consistent with typical observed cloud phase distribution. Moreover, the PH17 scheme is designed for bin microphysical schemes and is sensitive to the rimed fraction. However, in ICON's bulk microphysical scheme, the rimed fraction is not predicted but instead prescribed as a constant for different ice particles. The rimed fraction was set to 0.4 in this study, and a series of sensitivity experiments were performed using different values (0.2, 0.3, and 0.4). Different results on BR were observed but not significant. The finding aligns with Sotiropoulou et al. (2021a), who investigated the sensitivity of ice–ice collisions to ice habit, rimed fraction, and ice type in Arctic clouds. Nevertheless, using a constant rimed fraction for different colliding ice particles still introduces a certain degree of uncertainty.

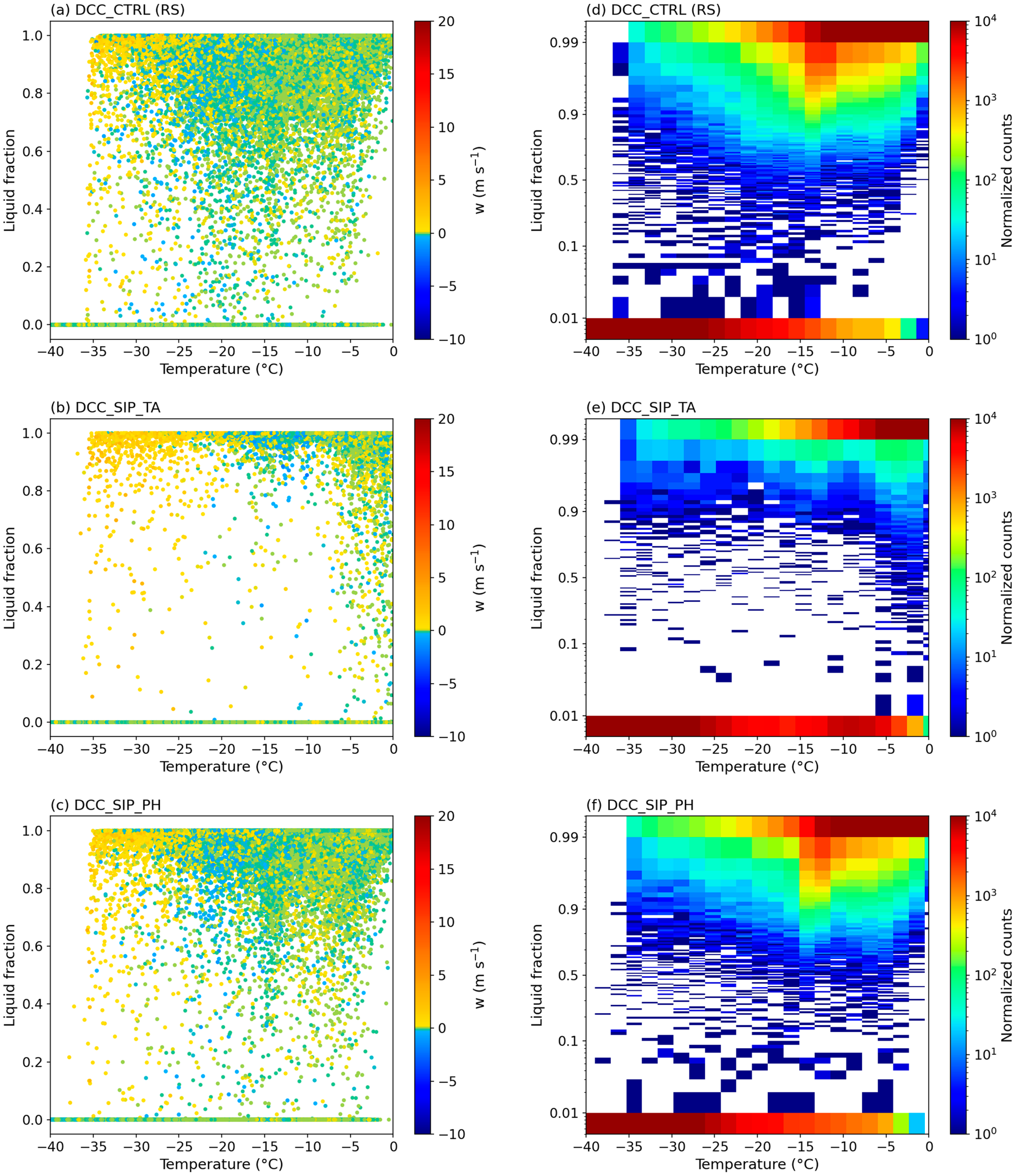

FIG. 8. Cloud-top supercooled liquid water mass fraction distribution as a function of temperature between 0900 and 1900 UTC for cases (a) DCC_CTRL, (b) DCC_SIP_TA, and (c) DCC_SIP_PH. The color of points indicates vertical velocity (m s^{-1}), warm colors represent ascending motion, while cool colors signify sinking motion. The 2D histogram of cloud-top liquid mass fraction vs temperature for cases (d) DCC_CTRL, (e) DCC_SIP_TA, and (f) DCC_SIP_PH. The temperature is binned by 1°C. The colors represent the normalized counts of data points (the number of data points is scaled to the [10^0, 10^4] range).

c. *Importance of cascade effects*

The cascade effect describes that the ice crystals produced by the SIP processes are involved again in the SIP processes. This process has attracted the attention of the cloud physics community (Koenig 1963; Lawson et al. 2015; Sullivan et al. 2018a) while it has not been investigated comprehensively. The same parameterization schemes for SIP were used in the DCC_SIP_PH and DCC_SIP_PH_NCS cases. However, new ice crystals produced by SIP processes were not reintroduced into the SIP processes in DCC_SIP_PH_NCS. Simulation results from the NWP DCC_SIP_PH, DCC_SIP_PH_NCS, and DCC_CTRL cases were compared to investigate the cascade effects on cloud microphysics. The ICNC is reduced to less than one-third (Fig. 10a), and the cloud ice mass mixing ratio (Fig. 10d) is almost halved due to switching off the cascade

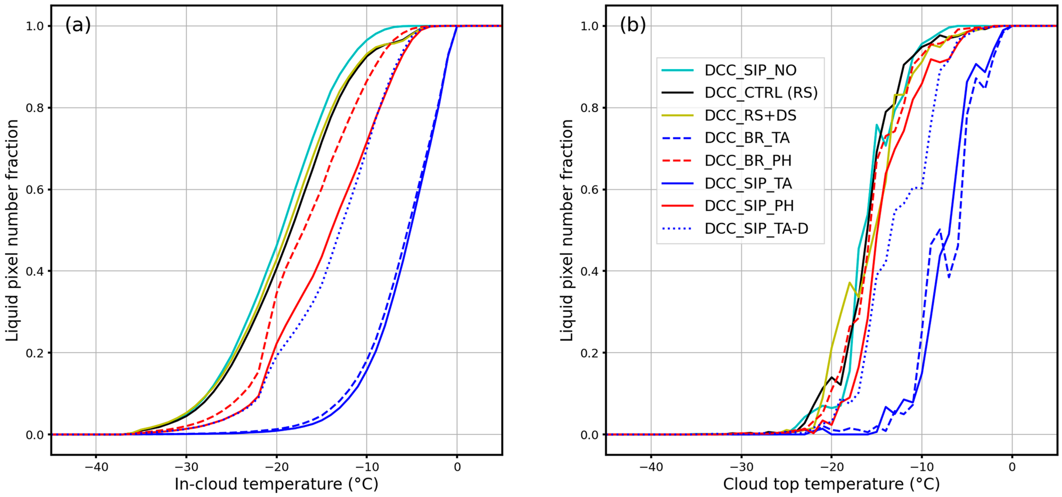

FIG. 9. Liquid cloud pixel number fraction as a function of temperature (binned by 1°C) from 0900 to 1900 UTC, (a) within the cloud and (b) at the cloud top.

effect. Due to the weak efficiency of ice crystal production without the cascade effect, cloud water number concentration and mass mixing ratio increase in the mixed-phase cloud layer (from 4 to 9 km) (Figs. 10b,e). Interestingly, rainwater is also increased in DCC_SIP_PH_NCS in the height range above 4 km compared to DCC_CTRL (Fig. 10f). The increase in rainwater in the mixed-phase layer is associated with intensified autoconversion and suppressed riming in DCC_SIP_PH_NCS (not shown). Note that switching off the cascade effect, the newly generated ice particles not only do not participate in the SIP process but also do not evolve in any other cloud microphysical processes either, such as WBF, ice aggregation, and sedimentation processes. Therefore, the differences in cloud hydrometeor number and mass mixing ratio shown in Fig. 10 might not be entirely caused by the cascade effect.

Process rates of RS, DS, and BR for DCC_SIP_PH and DCC_SIP_PH_NCS are shown in Fig. 11. Process rates of RS between DCC_SIP_PH and DCC_SIP_PH_NCS are comparable. This may be because the newly formed splinters do not grow fast enough in this temperature range to participate significantly in riming. The process rate of BR in DCC_SIP_PH_NCS is lower than that in DCC_SIP_PH by about two to three orders of magnitude throughout the entire vertical extent of the clouds. However, the process rate of DS in DCC_SIP_PH_NCS is slightly larger than that in DCC_SIP_PH. This is probably due to the increased rainwater in DCC_SIP_PH_NCS, leading to an enhanced DS process, and due to the fact that the DS process does not depend on the ICNC.

Yano and Phillips (2011) reported a regime for explosive ice multiplication resulting from ice–ice collisions with an ice enhancement ratio exceeding 10^4, which is attributed to the cascade effect. They proposed a dimensionless multiplication efficiency ($\tilde{c} = 4c_0 N \alpha \tau_f \tau_s$) to access the positive feedback of ice production due to SIP processes. In this study, following the theory by Yano and Phillips (2011), we estimated the dimensionless multiplication efficiency for snow–graupel collisions. The multiplication rate $N = 50$ was used in this study, which is the same as Yano and Phillips (2011). The volume sweep-out rate for snow is set to $\alpha = 2.4 \times 10^{-5}$ m^3 s^{-1}, which is the same as the value used by Yano and Phillips (2011) for graupel. Ice crystals grow into snow particles by depositional growth and aggregation over a time scale $\tau_s = 3$ min and the time scale for snowflakes lost from the cloud element due to gravitational fallout is about $\tau_f = 16.6$ min in this study. Thus, the substitution of parameters defined above into the equation leads to $\tilde{c} = 51.6$. The estimated multiplication efficiency in this study is smaller than the value (300) reported by Yano and Phillips (2011) but is still significantly higher than unity, indicating the potential for explosive multiplication.

d. *The ice enhancement factor*

The ice enhancement factor (IEF), also called the ice multiplication factor, is defined as the ratio of ice crystal number concentration to the primary ice number concentration (Wieder et al. 2022):

$$\mathrm{IEF} = \frac{\text{total ICNC}}{\text{primary ice}}. \tag{12}$$

The "total ICNC" is the number concentration of all types of ice particles. The "primary ice" includes ice particles produced via homogeneous freezing (only active below −38°C) and heterogeneous nucleation.

IEFs against temperature for the NWP sensitivity experiments are shown in Fig. 12. The peak values of IEF in DCC_CTRL and DCC_RS+DS are about 6 and are located at ∼−7°C, where the RS process is most active. Below −17°C, the IEF is almost equal to 1 in DCC_CTRL and is slightly larger than 1 in DCC_RS+DS. This indicates that the contribution of RS and DS processes to ice production is negligible below −15°C. IEF against temperature in DCC_SIP_PH has a bimodal structure, with the first peak at ∼−7°C and the second at ∼−24°C. The IEF value in the SIP_PH case is around 10 below −20°C and is as large as 200 at −24°C. The IEF value in DCC_BR_PH is

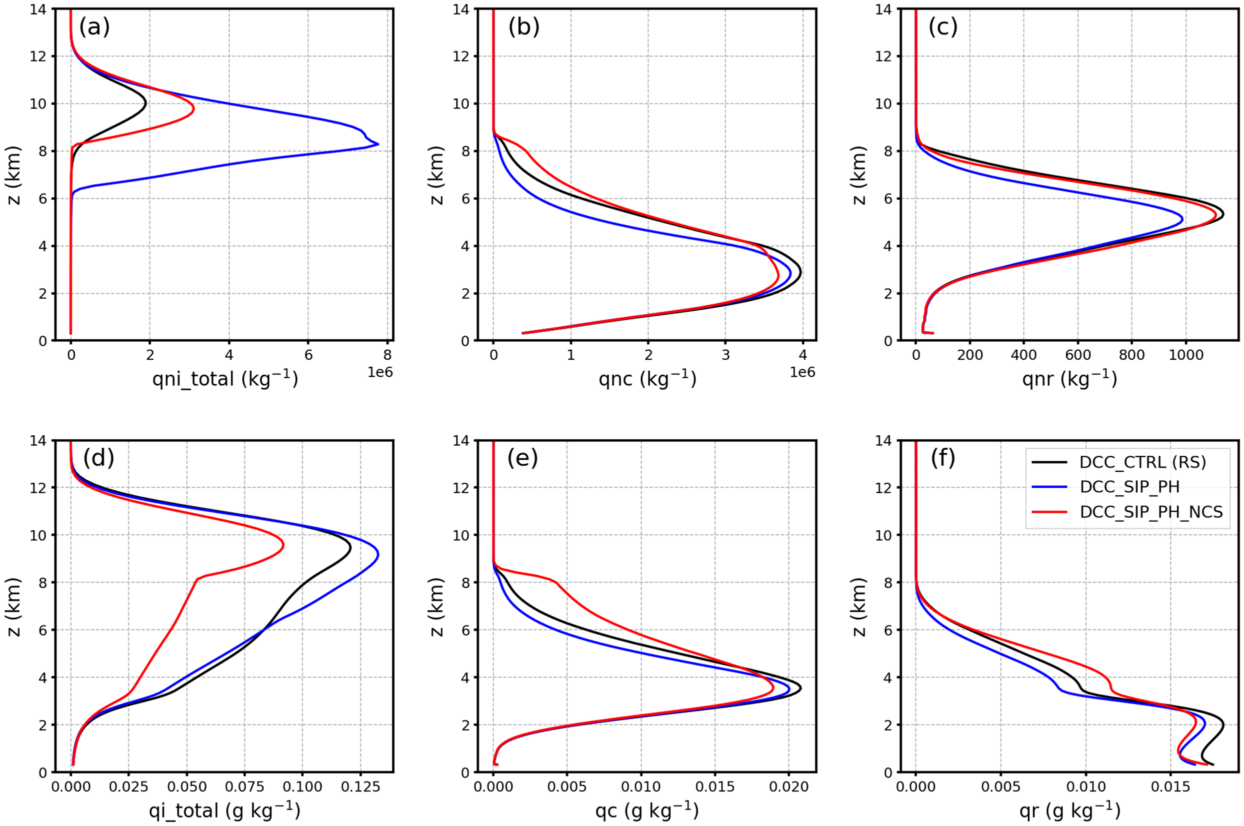

FIG. 10. Spatial and time-averaged (0900–1900 UTC) profiles of number concentration of (a) total cloud ice, (b) cloud liquid water, and (c) rainwater and profiles of mass mixing ratio of (d) total cloud ice, (e) cloud liquid water, and (f) rainwater for DCC_CTRL (black), DCC_SIP_TA (blue), and DCC_SIP_TA-NCS (red) cases.

smaller than that in DCC_SIP_PH in the temperature range between 0° and −17°C due to switching off RS and DS processes in DCC_BR_PH. The structure of IEF against temperature in DCC_SIP_TA-D is very similar to DCC_SIP_PH, while the IEF value is slightly smaller than DCC_SIP_PH, especially in the temperature range from 0° to −17°C. The range of values retrieved by Wieder et al. (2022) agrees with the DCC_SIP_PH and DCC_SIP_TA-D cases. Waman et al. (2022) reported recently that the IEF is on the order of 10^2–10^3 and is almost uniform over the entire simulation period of a continental convective storm. Thus, the magnitudes of IEF from this study are comparable to Waman et al.'s (2022) results. The contribution of RS and DS processes to ice crystal production is negligible compared to the BR process. The structures and values of IEF between DCC_SIP_TA and DCC_SIP_PH are significantly different due to different parameterization schemes for the BR process (not shown).

4. Summary and conclusions

In addition to RS, SIP from DS and BR processes has been implemented in ICON's two-moment cloud microphysical scheme to investigate the role of SIP for cloud microphysical properties and cloud phase distribution in continental deep convective clouds. The sensitivity of cloud microphysical properties and SIP efficiency to RS intensity and cascade effect was examined. Besides, uncertainties from different parameterization schemes for BR were investigated as well. Two types of simulations, NWP and LES, were performed to eliminate uncertainties introduced by model physics.

Cloud microphysical properties were modulated noticeably by including SIP processes. ICNCs increased by a factor of 4 (cases DCC_SIP_PH and DCC_SIP_TA-D) in the two cases implementing all three SIP processes. Surface precipitation decreased as much as 20% in DCC_SIP_PH and DCC_SIP_TA-D compared to the reference run (case DCC_CTRL). Interestingly, the BR process was found to dominate SIP, regardless of whether it was simulated by the TA95 scheme or the PH17 scheme. Analysis of cloud microphysical process rates indicates that the BR process rate is larger than RS and DS process rates by four and three orders of magnitude, respectively. There has been a long debate on which SIP process dominates the ice concentration. Studies by Phillips et al. (2017b) and Waman et al. (2022) are aligned with our findings that the BR process is the most prolific SIP mechanism in mature deep convective clouds. However, Waman et al. (2022) suggested that the RS process is ranked as first in the early growth stage of deep convective clouds. James et al. (2023) reported that the collision of supercooled water drops with ice particles is a more significant SIP mechanism in shallow convective clouds. Thus, the relative importance of SIP

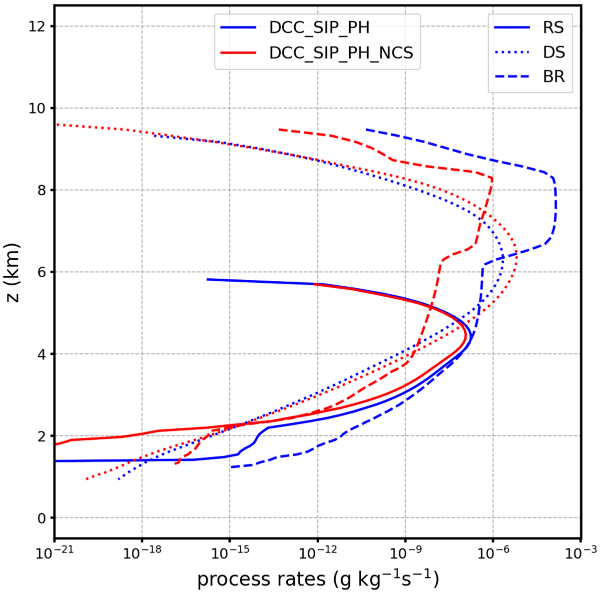

FIG. 11. Spatial and time-averaged (0900–1900 UTC) profiles of process rates of RS, DS, and BR for the NWP DCC_SIP_PH (blue) and DCC_SIP_PH_NCS (red) cases.

processes in producing ice crystals varies greatly with cloud types, temperature ranges, and stages of cloud development.

Cloud phase distributions, both inside clouds and at the cloud top, were influenced significantly by the SIP processes. Liquid and mixed-phase pixels decreased while ice pixels increased remarkably within the cloud and at the cloud top when SIP processes were implemented. In-cloud liquid pixel number fraction decreased significantly in the temperature range between −5° and −30°C when implementing all three SIP processes or only the BR process. The liquid pixel number fraction at the cloud top decreased unrealistically strong in the temperature range between 0° and −20°C when the TA95 scheme for BR was used, while in cases utilizing the PH17 scheme for BR and cases only implementing RS and DS processes, variations in liquid pixel number fractions were not pronounced. Thus, the BR process impacts cloud phase distributions the most out of the three SIP processes, and there are uncertainties in the parameterization of the BR process. For example, the applicability of the BR parameterization to collisions of ice particles of all size ranges or ice hydrometeor types, the collision kernels, possible turbulence effects, and the relative velocities all bring some degrees of uncertainty. Nevertheless, an increasing number of observational and simulation studies have confirmed the importance of implementing SIP parameterization in numerical models to enhance cloud microphysics simulations.

To further understand the importance of SIP processes, the influences of RS intensity and cascade effect on cloud microphysics were analyzed, and the IEF was also calculated. Scaling the RS intensity led to monotonic variations in ice crystal mass and number concentrations in the temperature range between −3° and −8°C. However, scaling RS intensity, even with a factor of 10, had limited impacts on ICNC and ice crystal mass mixing ratio. A novel approach was proposed to quantify the cascade effect as the difference between the full simulation and

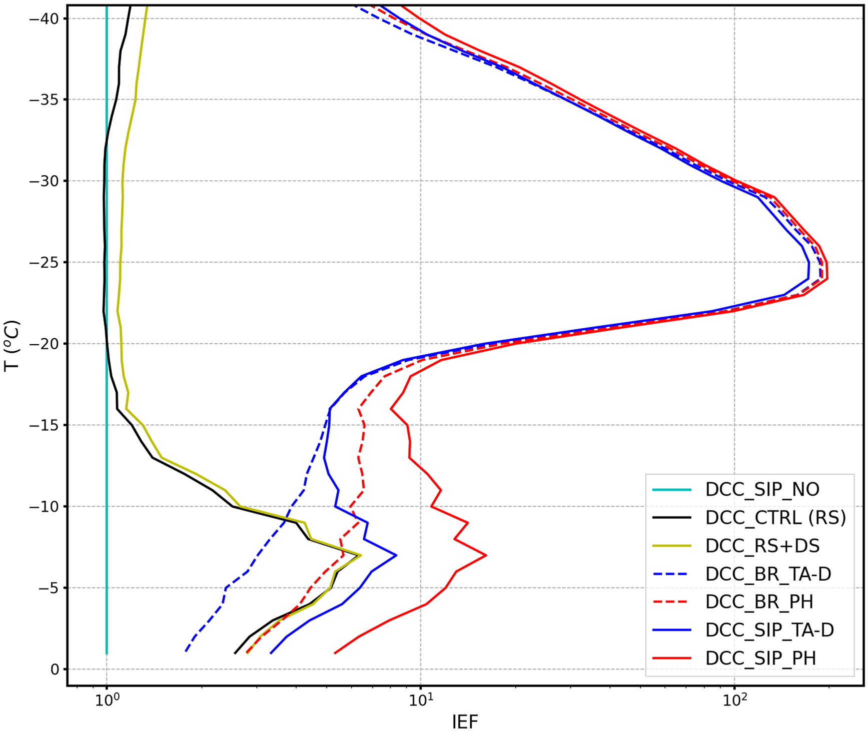

FIG. 12. Spatial and time-averaged (0900–1900 UTC) IEF against temperature for the NWP DCC cases.

a modified run, in which newly generated ice crystals from the SIP processes were not reintroduced into the SIP processes (cascade effect switched off). The cascade effect was found to be essential for SIP. Ice crystal mass and number concentrations decreased significantly when switching off the cascade effect, and the BR process rate was reduced by three orders of magnitude. Interestingly, supercooled liquid water increased in the mixed-phase cloud layer due to moderated SIP. The IEF was on the order of 10^2 in the simulated deep convective clouds. Yano and Phillips (2011) proposed a dimensionless multiplication efficiency to assess the positive feedback of ice production due to SIP processes. The estimated multiplication efficiency in this study is much higher than unity and is supposed to lead to an explosive multiplication. Moreover, the IEF increases to more than 10 typically within approximately 30 min in DCC_SIP_PH, DCC_SIP_TA-D, and DCC_BR_PH cases, where the BR process is included. Thus, simulation results in this study are consistent with Yano and Phillips's (2011) findings in their theoretical study.

In this study, SIP was verified to be important for cloud microphysics in continental deep convective clouds, and large uncertainties were found in the parameterizations of SIP processes. However, only the parameterization of RS has been widely used in numerical models. This suggests the necessity of including DS and BR parameterizations to account for SIP over a large temperature range in numerical models. A caveat is that the simulation results, for example, the ICNCs, are not evaluated against in situ observations in this study. However, parameterization schemes could be evaluated indirectly. For example, analysis on cloud phase distribution reveals that liquid cloud pixel number fraction simulated by the TA95 scheme (without diameter scaling) decreases significantly right below 0°C, which are not consistent with typical observed cloud phase distributions (Hoose et al. 2018; Bruno et al. 2021). It seems therefore likely that the TA95 scheme is too active. Besides, other than in situ observations, satellite datasets, for example, cloud-top temperature and cloud-top phase distribution from the SEVIRI data (Han et al. 2023), could also be used to evaluate the parameterization schemes, although they are not particularly strong constraints.

Acknowledgments. This project has received funding from the European Research Council (ERC) under the European Union's Horizon 2020 research and innovation programme under Grant Agreements 714062 (ERC Starting Grant "C2Phase") and 821205 ("FORCeS"). We gratefully acknowledge the computing time provided by the German Climate Computing Centre (DKRZ) on the HPC system Levante and the Steinbuch Centre for Computing (SCC) on the HPC system HoreKa.

Data availability statement. The data that support the findings of this study are available from the corresponding author upon reasonable request.

APPENDIX

Collisional Breakup Parameterization by PH17

The PH17 parameterization scheme allows for varying treatments of $\aleph_{\mathrm{BR}}$ depending on the ice crystal type and habit. The parameterization of fragment number $\aleph_{\mathrm{BR}}$, collision kinetic energy K_0, and characteristic collision velocity difference have already been introduced in section 2b(3). Here, detailed parameters in Eqs. (9) and (10) are introduced. The term A represents the number density of the breakable asperities in the region of contact. The term C is the asperity-fragility coefficient, which is a function of a correction term ψ for the effects of sublimation based on the field observations by Vardiman (1978). Exponent γ is a function of rimed fraction for collisions that include cloud ice and snow.

For collisions of either nondendritic planar ice or snow (with rimed fraction $\Psi < 0.5$) with any ice particles (snow, graupel, or hail),

$$A = 1.58 \times 10^7(1 + 100\Psi^2)\left(1 + \frac{1.33 \times 10^{-4}}{D^{1.5}}\right), \tag{A1}$$

$$C = 7.08 \times 10^6 \times \psi$$
$$\psi = 3.5 \times 10^{-3}$$
$$\gamma = 0.5\text{–}0.25\Psi.$$

For collisions of dendritic ice or snow (with rimed fraction $\Psi < 0.5$) with any ice particles (snow, graupel, or hail), parameters A and C are changed:

$$A = 1.41 \times 10^6(1 + 100\Psi^2)\left(1 + \frac{3.98 \times 10^{-5}}{D^{1.5}}\right), \tag{A2}$$

$$C = 3.09 \times 10^6 \times \psi$$
$$\psi = 3.5 \times 10^{-3}$$
$$\gamma = 0.5 - 0.25\Psi.$$

For collisions of graupel with graupel or hail, parameters are different:

$$A = \frac{a_0}{3} + \max\left(\frac{2a_0}{3} - \frac{a_0}{9}|T - T_0|, 0\right), \tag{A3}$$

$$a_0 = 3.78 \times 10^6\left(1 + \frac{0.0079}{D^{1.5}}\right)$$
$$C = 6.3 \times 10^6 \times \psi$$
$$\psi = 3.5 \times 10^{-3}$$
$$\gamma = 0.3.$$

Those parameters were evaluated based on ice particles with diameters between 0.5 and 5 mm. However, PH17a pointed out that the parameters can also be used for particle sizes outside the recommended range, as long as the input variables to the scheme are set to the nearest limit of the range.

REFERENCES

Atlas, R. L., C. S. Bretherton, M. F. Khairoutdinov, and P. N. Blossey, 2022: Hallett-Mossop rime splintering dims cumulus clouds over the Southern Ocean: New insight from nudged global storm-resolving simulations. *AGU Adv.*, **3**, e2021AV000454, https://doi.org/10.1029/2021AV000454.

Benas, N., S. Finkensieper, M. Stengel, G.-J. van Zadelhoff, T. Hanschmann, R. Hollmann, and J. F. Meirink, 2017: The MSG-SEVIRI-based cloud property data record CLAAS-2. *Earth Syst. Sci. Data*, **9**, 415–434, https://doi.org/10.5194/essd-9-415-2017.

Bower, K. N., S. J. Moss, D. W. Johnson, T. W. Choularton, J. Latham, P. R. A. Brown, A. M. Blyth, and J. Cardwell, 1996: A parametrization of the ice water content observed in frontal and convective clouds. *Quart. J. Roy. Meteor. Soc.*, **122**, 1815–1844, https://doi.org/10.1002/qj.49712253605.

Bruno, O., C. Hoose, T. Storelvmo, Q. Coopman, and M. Stengel, 2021: Exploring the cloud top phase partitioning in different cloud types using active and passive satellite sensors., *Geophys. Res. Lett.*, **48**, e2020GL089863, https://doi.org/10.1029/2020GL089863.

Coopman, Q., C. Hoose, and M. Stengel, 2020: Analysis of the thermodynamic phase transition of tracked convective clouds based on geostationary satellite observations. *J. Geophys. Res. Atmos.*, **125**, e2019JD032146, https://doi.org/10.1029/2019JD032146.

——, ——, and ——, 2021: Analyzing the thermodynamic phase partitioning of mixed phase clouds over the Southern Ocean using passive satellite observations. *Geophys. Res. Lett.*, **48**, e2021GL093225, https://doi.org/10.1029/2021GL093225.

Dedekind, Z., A. Lauber, S. Ferrachat, and U. Lohmann, 2021: Sensitivity of precipitation formation to secondary ice production in winter orographic mixed-phase clouds. *Atmos. Chem. Phys.*, **21**, 15 115–15 134, https://doi.org/10.5194/acp-21-15115-2021.

Dipankar, A., B. Stevens, R. Heinze, C. Moseley, G. Zängl, M. Giorgetta, and S. Brdar, 2015: Large eddy simulation using the general circulation model ICON. *J. Adv. Model. Earth Syst.*, **7**, 963–986, https://doi.org/10.1002/2015MS000431.

Dye, J. E., and P. V. Hobbs, 1968: The influence of environmental parameters on the freezing and fragmentation of suspended water drops. *J. Atmos. Sci.*, **25**, 82–96, https://doi.org/10.1175/1520-0469(1968)025<0082:TIOEPO>2.0.CO;2.

Field, P. R., and Coauthors, 2017: Secondary ice production: Current state of the science and recommendations for the future. *Ice Formation and Evolution in Clouds and Precipitation: Measurement and Modeling Challenges*, *Meteor. Monogr.*, No. 58, Amer. Meteor. Soc., https://doi.org/10.1175/AMSMONOGRAPHS-D-16-0014.1.

Fridlind, A. M., A. S. Ackerman, G. McFarquhar, G. Zhang, M. R. Poellot, P. J. DeMott, A. J. Prenni, and A. J. Heymsfield, 2007: Ice properties of single-layer stratocumulus during the mixed-phase Arctic cloud experiment: 2. Model results. *J. Geophys. Res.*, **112**, D24202, https://doi.org/10.1029/2007JD008646.

Fu, S., X. Deng, M. D. Shupe, and H. Xue, 2019: A modelling study of the continuous ice formation in an autumnal Arctic mixed-phase cloud case. *Atmos. Res.*, **228**, 77–85, https://doi.org/10.1016/j.atmosres.2019.05.021.

Gassmann, A., and H.-J. Herzog, 2008: Towards a consistent numerical compressible non-hydrostatic model using generalized Hamiltonian tools. *Quart. J. Roy. Meteor. Soc.*, **134**, 1597–1613, https://doi.org/10.1002/qj.297.

Georgakaki, P., G. Sotiropoulou, É. Vignon, A.-C. Billault-Roux, A. Berne, and A. Nenes, 2022: Secondary ice production processes in wintertime alpine mixed-phase clouds. *Atmos. Chem. Phys.*, **22**, 1965–1988, https://doi.org/10.5194/acp-22-1965-2022.

Gold, L. W., 1963: Crack formation in ice plates by thermal shock. *Can. J. Phys.*, **41**, 1712–1728, https://doi.org/10.1139/p63-172.

Gupta, A. K., and Coauthors, 2023: The microphysics of the warm-rain and ice crystal processes of precipitation in simulated continental convective storms. *Commun. Earth Environ.*, **4**, 226, https://doi.org/10.1038/s43247-023-00884-5.

Hallett, J., and S. C. Mossop, 1974: Production of secondary ice particles during the riming process. *Nature*, **249**, 26–28, https://doi.org/10.1038/249026a0.

Han, C., C. Hoose, M. Stengel, Q. Coopman, and A. Barrett, 2023: Sensitivity of cloud-phase distribution to cloud microphysics and thermodynamics in simulated deep convective clouds and SEVIRI retrievals. *Atmos. Chem. Phys.*, **23**, 14 077–14 095, https://doi.org/10.5194/acp-23-14077-2023.

Hande, L. B., C. Engler, C. Hoose, and I. Tegen, 2015: Seasonal variability of Saharan desert dust and ice nucleating particles over Europe. *Atmos. Chem. Phys.*, **15**, 4389–4397, https://doi.org/10.5194/acp-15-4389-2015.

——, ——, ——, and ——, 2016: Parameterizing cloud condensation nuclei concentrations during HOPE. *Atmos. Chem. Phys.*, **16**, 12 059–12 079, https://doi.org/10.5194/acp-16-12059-2016.

Harris-Hobbs, R. L., and W. A. Cooper, 1987: Field evidence supporting quantitative predictions of secondary ice production rates. *J. Atmos. Sci.*, **44**, 1071–1082, https://doi.org/10.1175/1520-0469(1987)044<1071:FESQPO>2.0.CO;2.

Heymsfield, A. J., and M. Kajikawa, 1987: An improved approach to calculating terminal velocities of plate-like crystals and graupel. *J. Atmos. Sci.*, **44**, 1088–1099, https://doi.org/10.1175/1520-0469(1987)044<1088:AIATCT>2.0.CO;2.

Hoarau, T., J.-P. Pinty, and C. Barthe, 2018: A representation of the collisional ice break-up process in the two-moment microphysics LIMA v1.0 scheme of Meso-NH. *Geosci. Model Dev.*, **11**, 4269–4289, https://doi.org/10.5194/gmd-11-4269-2018.

Hoose, C., M. Karrer, and C. Barthlott, 2018: Cloud top phase distributions of simulated deep convective clouds. *J. Geophys. Res. Atmos.*, **123**, 10 464–10 476, https://doi.org/10.1029/2018JD028381.

Huang, Y., and Coauthors, 2022: Microphysical processes producing High Ice Water Contents (HIWCs) in tropical convective clouds during the HAIC-HIWC field campaign: Dominant role of secondary ice production. *Atmos. Chem. Phys.*, **22**, 2365–2384, https://doi.org/10.5194/acp-22-2365-2022.

Jackson, R., J. R. French, D. C. Leon, D. M. Plummer, S. Lasher-Trapp, A. M. Blyth, and A. Korolev, 2018: Observations of the microphysical evolution of convective clouds in the southwest of the United Kingdom. *Atmos. Chem. Phys.*, **18**, 15 329–15 344, https://doi.org/10.5194/acp-18-15329-2018.

James, R. L., V. T. J. Phillips, and P. J. Connolly, 2021: Secondary ice production during the break-up of freezing water drops on impact with ice particles. *Atmos. Chem. Phys.*, **21**, 18 519–18 530, https://doi.org/10.5194/acp-21-18519-2021.

——, J. Crosier, and P. J. Connolly, 2023: A bin microphysics parcel model investigation of secondary ice formation in an idealised shallow convective cloud. *Atmos. Chem. Phys.*, **23**, 9099–9121, https://doi.org/10.5194/acp-23-9099-2023.

Kärcher, B., J. Hendricks, and U. Lohmann, 2006: Physically based parameterization of cirrus cloud formation for use in global atmospheric models. *J. Geophys. Res.*, **111**, D01205, https://doi.org/10.1029/2005JD006219.

Keinert, A., D. Spannagel, T. Leisner, and A. Kiselev, 2020: Secondary ice production upon freezing of freely falling drizzle droplets. *J. Atmos. Sci.*, **77**, 2959–2967, https://doi.org/10.1175/JAS-D-20-0081.1.

Koenig, L. R., 1963: The glaciating behavior of small cumulonimbus clouds. *J. Atmos. Sci.*, **20**, 29–47, https://doi.org/10.1175/1520-0469(1963)020<0029:TGBOSC>2.0.CO;2.

——, and F. W. Murray, 1977: The rime-splintering hypothesis of cumulus glaciation examined using a field-of-flow cloud model. *Quart. J. Roy. Meteor. Soc.*, **103**, 585–606, https://doi.org/10.1002/qj.49710343805.

Korolev, A., and T. Leisner, 2020: Review of experimental studies of secondary ice production. *Atmos. Chem. Phys.*, **20**, 11 767–11 797, https://doi.org/10.5194/acp-20-11767-2020.

——, and Coauthors, 2017: Mixed-phase clouds: Progress and challenges. *Ice Formation and Evolution in Clouds and Precipitation: Measurement and Modeling Challenges*, *Meteor. Monogr.*, No. 58, Amer. Meteor. Soc., https://doi.org/10.1175/AMSMONOGRAPHS-D-17-0001.1.

Korolev, A. V., G. A. Isaac, S. G. Cober, J. W. Strapp, and J. Hallett, 2003: Microphysical characterization of mixed-phase clouds. *Quart. J. Roy. Meteor. Soc.*, **129**, 39–65, https://doi.org/10.1256/qj.01.204.

Lasher-Trapp, S., S. Kumar, D. H. Moser, A. M. Blyth, J. R. French, R. C. Jackson, D. C. Leon, and D. M. Plummer, 2018: On different microphysical pathways to convective rainfall. *J. Appl. Meteor. Climatol.*, **57**, 2399–2417, https://doi.org/10.1175/JAMC-D-18-0041.1.

——, E. L. Scott, E. Järvinen, M. Schnaiter, F. Waitz, P. J. DeMott, C. S. McCluskey, and T. C. J. Hill, 2021: Observations and modeling of rime splintering in Southern Ocean cumuli. *J. Geophys. Res. Atmos.*, **126**, e2021JD035479, https://doi.org/10.1029/2021JD035479.

Latham, J., and B. J. Mason, 1961: Generation of electric charge associated with the formation of soft hail in thunderclouds. *Proc. Roy. Soc. London*, **A260**, 537–549, https://doi.org/10.1098/rspa.1961.0052.

Lauber, A., A. Kiselev, T. Pander, P. Handmann, and T. Leisner, 2018: Secondary ice formation during freezing of levitated droplets. *J. Atmos. Sci.*, **75**, 2815–2826, https://doi.org/10.1175/JAS-D-18-0052.1.

——, J. Henneberger, C. Mignani, F. Ramelli, J. T. Pasquier, J. Wieder, M. Hervo, and U. Lohmann, 2021: Continuous secondary-ice production initiated by updrafts through the melting layer in mountainous regions. *Atmos. Chem. Phys.*, **21**, 3855–3870, https://doi.org/10.5194/acp-21-3855-2021.

Lawson, R. P., S. Woods, and H. Morrison, 2015: The microphysics of ice and precipitation development in tropical cumulus clouds. *J. Atmos. Sci.*, **72**, 2429–2445, https://doi.org/10.1175/JAS-D-14-0274.1.

Leon, D. C., and Coauthors, 2016: The Convective Precipitation Experiment (COPE): Investigating the origins of heavy precipitation in the southwestern United Kingdom. *Bull. Amer. Meteor. Soc.*, **97**, 1003–1020, https://doi.org/10.1175/BAMS-D-14-00157.1.

Lilly, D. K., 1962: On the numerical simulation of buoyant convection. *Tellus*, **14A**, 148–172, https://doi.org/10.3402/tellusa.v14i2.9537.

Locatelli, J. D., and P. V. Hobbs, 1974: Fall speeds and masses of solid precipitation particles. *J. Geophys. Res.*, **79**, 2185–2197, https://doi.org/10.1029/JC079i015p02185.

Luke, E. P., F. Yang, P. Kollias, A. M. Vogelmann, and M. Maahn, 2021: New insights into ice multiplication using remote-sensing observations of slightly supercooled mixed-phase clouds in the Arctic. *Proc. Natl. Acad. Sci. USA*, **118**, e2021387118, https://doi.org/10.1073/pnas.2021387118.

McCoy, D. T., I. Tan, D. L. Hartmann, M. D. Zelinka, and T. Storelvmo, 2016: On the relationships among cloud cover, mixed-phase partitioning, and planetary albedo in GCMs. *J. Adv. Model. Earth Syst.*, **8**, 650–668, https://doi.org/10.1002/2015MS000589.

Miltenberger, A. K., T. Lüttmer, and C. Siewert, 2020: Secondary ice formation in idealised deep convection—Source of primary ice and impact on glaciation. *Atmosphere*, **11**, 542, https://doi.org/10.3390/atmos11050542.

Oraltay, R. G., and J. Hallett, 1989: Evaporation and melting of ice crystals: A laboratory study. *Atmos. Res.*, **24**, 169–189, https://doi.org/10.1016/0169-8095(89)90044-6.

Pasquier, J. T., and Coauthors, 2022: Conditions favorable for secondary ice production in Arctic mixed-phase clouds. *Atmos. Chem. Phys.*, **22**, 15 579–15 601, https://doi.org/10.5194/acp-22-15579-2022.

Patade, S., and Coauthors, 2022: The influence of multiple groups of biological ice nucleating particles on microphysical properties of mixed-phase clouds observed during MC3E. *Atmos. Chem. Phys.*, **22**, 12 055–12 075, https://doi.org/10.5194/acp-22-12055-2022.

Phillips, V. T. J., J.-I. Yano, and A. Khain, 2017a: Ice multiplication by breakup in ice–ice collisions. Part I: Theoretical formulation. *J. Atmos. Sci.*, **74**, 1705–1719, https://doi.org/10.1175/JAS-D-16-0224.1.

——, and Coauthors, 2017b: Ice multiplication by breakup in ice–ice collisions. Part II: Numerical simulations. *J. Atmos. Sci.*, **74**, 2789–2811, https://doi.org/10.1175/JAS-D-16-0223.1.

——, S. Patade, J. Gutierrez, and A. Bansemer, 2018: Secondary ice production by fragmentation of freezing drops: Formulation and theory. *J. Atmos. Sci.*, **75**, 3031–3070, https://doi.org/10.1175/JAS-D-17-0190.1.

Rosenfeld, D., and Coauthors, 2011: Glaciation temperatures of convective clouds ingesting desert dust, air pollution and smoke from forest fires. *Geophys. Res. Lett.*, **38**, L21804, https://doi.org/10.1029/2011GL049423.

Seifert, A., and K. D. Beheng, 2006: A two-moment cloud microphysics parameterization for mixed-phase clouds. Part 1: Model description. *Meteor. Atmos. Phys.*, **92**, 45–66, https://doi.org/10.1007/s00703-005-0112-4.

Sotiropoulou, G., S. Sullivan, J. Savre, G. Lloyd, T. Lachlan-Cope, A. M. L. Ekman, and A. Nenes, 2020: The impact of secondary ice production on Arctic stratocumulus. *Atmos. Chem. Phys.*, **20**, 1301–1316, https://doi.org/10.5194/acp-20-1301-2020.

——, L. Ickes, A. Nenes, and A. M. L. Ekman, 2021a: Ice multiplication from ice–ice collisions in the high Arctic: Sensitivity to ice habit, rimed fraction, ice type and uncertainties in the numerical description of the process. *Atmos. Chem. Phys.*, **21**, 9741–9760, https://doi.org/10.5194/acp-21-9741-2021.

——, É. Vignon, G. Young, H. Morrison, S. J. O'Shea, T. Lachlan-Cope, A. Berne, and A. Nenes, 2021b: Secondary ice production in summer clouds over the Antarctic coast: An underappreciated process in atmospheric models. *Atmos. Chem. Phys.*, **21**, 755–771, https://doi.org/10.5194/acp-21-755-2021.

Stengel, M., A. Kniffka, J. F. Meirink, M. Lockhoff, J. Tan, and R. Hollmann, 2014: CLAAS: The CM SAF cloud property data set using SEVIRI. *Atmos. Chem. Phys.*, **14**, 4297–4311, https://doi.org/10.5194/acp-14-4297-2014.

Sullivan, S. C., C. Hoose, and A. Nenes, 2017: Investigating the contribution of secondary ice production to in-cloud ice crystal numbers. *J. Geophys. Res. Atmos.*, **122**, 9391–9412, https://doi.org/10.1002/2017JD026546.

——, C. Barthlott, J. Crosier, I. Zhukov, A. Nenes, and C. Hoose, 2018a: The effect of secondary ice production parameterization on the simulation of a cold frontal rainband. *Atmos. Chem. Phys.*, **18**, 16 461–16 480, https://doi.org/10.5194/acp-18-16461-2018.

——, C. Hoose, A. Kiselev, T. Leisner, and A. Nenes, 2018b: Initiation of secondary ice production in clouds. *Atmos. Chem. Phys.*, **18**, 1593–1610, https://doi.org/10.5194/acp-18-1593-2018.

Takahashi, C., and A. Yamashita, 1970: Shattering of frozen water drops in a supercooled cloud. *J. Meteor. Soc. Japan*, **48**, 373–376, https://doi.org/10.2151/jmsj1965.48.4_373.

Takahashi, T., Y. Nagao, and Y. Kushiyama, 1995: Possible high ice particle production during graupel–graupel collisions. *J. Atmos. Sci.*, **52**, 4523–4527, https://doi.org/10.1175/1520-0469(1995)052<4523:PHIPPD>2.0.CO;2.

Taylor, J. W., and Coauthors, 2016: Observations of cloud microphysics and ice formation during COPE. *Atmos. Chem. Phys.*, **16**, 799–826, https://doi.org/10.5194/acp-16-799-2016.

Vardiman, L., 1978: The generation of secondary ice particles in clouds by crystal–crystal collision. *J. Atmos. Sci.*, **35**, 2168–2180, https://doi.org/10.1175/1520-0469(1978)035<2168:TGOSIP>2.0.CO;2.

Waman, D., S. Patade, A. Jadav, A. Deshmukh, A. K. Gupta, V. T. J. Phillips, A. Bansemer, and P. J. DeMott, 2022: Dependencies of four mechanisms of secondary ice production on cloud-top temperature in a continental convective storm. *J. Atmos. Sci.*, **79**, 3375–3404, https://doi.org/10.1175/JAS-D-21-0278.1.

——, A. Deshmukh, A. Jadav, S. Patade, M. Gautam, V. Phillips, A. Bansemer, and J. Jakobsson, 2023: Effects from time dependence of ice nucleus activity for contrasting cloud types. *J. Atmos. Sci.*, **80**, 2013–2039, https://doi.org/10.1175/JAS-D-22-0187.1.

Wan, H., and Coauthors, 2013: The ICON-1.2 hydrostatic atmospheric dynamical core on triangular grids—Part 1: Formulation and performance of the baseline version. *Geosci. Model Dev.*, **6**, 735–763, https://doi.org/10.5194/gmd-6-735-2013.

Wieder, J., and Coauthors, 2022: Retrieving ice-nucleating particle concentration and ice multiplication factors using active remote sensing validated by in situ observations. *Atmos. Chem. Phys.*, **22**, 9767–9797, https://doi.org/10.5194/acp-22-9767-2022.

Yano, J.-I., and V. T. J. Phillips, 2011: Ice–ice collisions: An ice multiplication process in atmospheric clouds. *J. Atmos. Sci.*, **68**, 322–333, https://doi.org/10.1175/2010JAS3607.1.

Zängl, G., D. Reinert, P. Rípodas, and M. Baldauf, 2015: The ICON (ICOsahedral Non-hydrostatic) modelling framework of DWD and MPI-M: Description of the non-hydrostatic dynamical core. *Quart. J. Roy. Meteor. Soc.*, **141**, 563–579, https://doi.org/10.1002/qj.2378.

Zhao, X., and X. Liu, 2021: Global importance of secondary ice production. *Geophys. Res. Lett.*, **48**, e2021GL092581, https://doi.org/10.1029/2021GL092581.

——, ——, V. T. J. Phillips, and S. Patade, 2021: Impacts of secondary ice production on Arctic mixed-phase clouds based on ARM observations and CAM6 single-column model simulations. *Atmos. Chem. Phys.*, **21**, 5685–5703, https://doi.org/10.5194/acp-21-5685-2021.